



OPEN ACCESS

EDITED BY

Anabela Oliveira,
Instituto Hidrográfico, Portugal

REVIEWED BY

Cristina Roque,
Estrutura de Missão para a Extensão da
Plataforma Continental, Portugal
Gemma Aiello,
National Research Council (CNR), Italy
Zhuangcai Tian,
China University of Mining and
Technology, China

*CORRESPONDENCE

Adrián López-Quirós,
✉ alquiros@ugr.es

RECEIVED 20 March 2025

ACCEPTED 08 July 2025

PUBLISHED 30 July 2025

CITATION

López-Quirós A, Puga-Bernabéu Á, Lobo FJ,
Ruiz-Caballero E, Cerrillo-Escoriza J,
Pérez-Asensio JN, Mendes I, Mena A,
Puche-Polo N, Alberjón-Peñas T and
Wacker L (2025) Western Mediterranean
shelf-incised submarine canyons: multi-proxy
evidence of Late Holocene natural and
human-induced environmental changes.
Front. Earth Sci. 13:1597056.
doi: 10.3389/feart.2025.1597056

COPYRIGHT

© 2025 López-Quirós, Puga-Bernabéu, Lobo,
Ruiz-Caballero, Cerrillo-Escoriza,
Pérez-Asensio, Mendes, Mena, Puche-Polo,
Alberjón-Peñas and Wacker. This is an
open-access article distributed under the
terms of the [Creative Commons Attribution
License \(CC BY\)](https://creativecommons.org/licenses/by/4.0/). The use, distribution or
reproduction in other forums is permitted,
provided the original author(s) and the
copyright owner(s) are credited and that the
original publication in this journal is cited, in
accordance with accepted academic practice.
No use, distribution or reproduction is
permitted which does not comply with
these terms.

Western Mediterranean shelf-incised submarine canyons: multi-proxy evidence of Late Holocene natural and human-induced environmental changes

Adrián López-Quirós^{1*}, Ángel Puga-Bernabéu¹,
Francisco José Lobo², Elvira Ruiz-Caballero^{1,3},
Javier Cerrillo-Escoriza⁴, José N. Pérez-Asensio¹,
Isabel Mendes⁵, Anxo Mena⁶, Natalia Puche-Polo^{1,7},
Tomás Alberjón-Peñas^{1,7} and Lukas Wacker⁸

¹Department of Stratigraphy and Paleontology, Facultad de Ciencias, Universidad de Granada, Granada, Spain, ²Instituto Andaluz de Ciencias de la Tierra (IACT-CSIC), Armilla, Spain, ³Grupo de Recursos Hídricos y Geología Ambiental, Departamento de Biología y Geología, Universidad de Almería, Almería, Spain, ⁴Instituto Español de Oceanografía, Centro Oceanográfico de Málaga (IEO-CSIC), Málaga, Spain, ⁵Centre for Marine and Environmental Research/Aquatic Research Network (CIMA/ARNET), Universidade do Algarve, Faro, Portugal, ⁶Departamento de Xeociencias Mariñas e Ordenación do Territorio, Facultad de Ciencias do Mar Edif, CC Experimentais Campus Universitario, Universidad de Vigo, Vigo, Spain, ⁷Unitat d'Estratigrafia, Departament de Geologia, Facultat de Ciències, Universitat Autònoma de Barcelona, Bellaterra, Spain, ⁸Laboratory of Ion Beam Physics, ETH Zürich, Zürich, Switzerland

Submarine canyons play a critical role in continental margin sediment transport, functioning both as sediment traps and conduits. This study examines the depositional dynamics of the Motril, Carchuna, and Calahonda canyons in the northern Alboran Sea (western Mediterranean) to assess their role in Holocene sediment storage and transfer. Comprehensive sedimentological and elemental geochemical analyses reveal distinct sedimentation patterns driven by geomorphology, diverse transport mechanisms, and hydroclimatic variability. The Motril Canyon primarily functioned as a river-fed sediment trap, accumulating fine-grained terrigenous material from the Guadalfeo River. At the same time, the Carchuna Canyon was dominated by longshore drift and turbidity currents mobilizing coarse-grained sediments. In contrast, the Calahonda Canyon displays an intermediate behavior, influenced by alongshore drift and fluvial inputs. The Late Holocene sedimentary record from the Motril Canyon provides a high-resolution sedimentary archive of paleoenvironmental changes over the last ~2000 years Current Era, reflecting both climatic variability and human-induced landscape alterations. Four phases are identified based on the relationships between sediment physical and mineral-chemical characteristics: the Iberian Roman Humid Period (2600–1600 cal. yr Before Present), characterized by diminished terrigenous input despite increased late-phase humidity; the Dark Ages (1500–1000 cal. yr BP), marked by elevated sedimentation linked to soil erosion

and intensified land use; the Medieval Climate Anomaly (1050–650 cal. yr BP), where persistent fine-grained deposition was driven largely by anthropogenic land degradation; and the Little Ice Age (650–150 cal. yr BP), which witnessed heightened sedimentation due to increased rainfall and river discharge. A decline in fluvial-derived material during the Industrial Period indicates a shift towards overall drier conditions, associated with changes in precipitation patterns and land use. These findings underscore the interplay between natural climatic fluctuations and human activities influencing western Mediterranean margin sedimentation. While the Motril Canyon does not serve as a direct conduit to deep waters, it nonetheless records the progressive aridification and anthropogenic impacts experienced in southern Iberia. Furthermore, the contrasting sediment dynamics observed in the Carchuna and Calahonda canyons highlight the inherent complexity of shelf-to-slope sediment transfer. This complexity underlines the necessity to consider human influences when interpreting Late Holocene paleoenvironmental records.

KEYWORDS

submarine canyons, sediment analysis, XRF element ratios, sediment transport, climate dynamics, Northern Alboran Sea

1 Introduction

Continental shelves and slopes constitute the genetically related middle segment of source-to-sink systems across continental margins. They are crucial for understanding land-ocean mass transfer as they contain a valuable record of sedimentary processes that have operated at different temporal and spatial scales (Sømme et al., 2009). The shelf is a key part of the transport pathway in routing sediments from the catchments to the continental slope, as it controls the amount of sediment stored *versus* delivered (Olariu and Steel, 2009). Submarine canyons are a common morphological feature in continental margins (e.g., Normark and Carlson, 2003; Harris and Whiteway, 2011). Their morphology and evolution result from the interplay of multiple sedimentary, oceanographic, and tectonic processes. Among the primary mechanisms controlling submarine canyon formation are turbidity currents and slope failures, which actively shape their structure and promote downslope sediment transport (e.g., Shepard, 1981; Talling et al., 2022). One of the most important processes responsible for the formation of submarine canyons involves retrogressive failures leading into the channelization of sediment gravity flows by pathways of preferential erosion (Pratson and Coakley, 1996). In active continental margins, tectonic activity and volcanism also influence canyon morphology and incision patterns (e.g., Aiello et al., 2020; Fogliini et al., 2025). A variety of processes can drive the initiation and maintenance of turbidity currents within canyons, including fluvially derived hyperpycnal flows (Mas et al., 2010; Martínez-Lamas et al., 2020), storm-induced sediment remobilization (Paull et al., 2011; Xu et al., 2013; Bosman et al., 2020), and enhanced off-shelf advection (e.g., Palanques et al., 2008). In addition, sediment failures involving recently deposited fluvial material (e.g., Mas et al., 2010) or mass wasting along canyon flanks (e.g., Micallef et al., 2012) can also trigger gravity flows. Oceanographic processes such as dense shelf-water cascading (Palanques et al., 2012; Saldías and Allen, 2020) and internal wave activity (Puig et al., 2004; 2013; 2014) further contribute to sediment

resuspension, entrainment, and transport within canyons. These combined mechanisms highlight the complex and dynamic role that submarine canyons play as the primary conduits for shelf-to-basin sediment transport (Shepard, 1981; Canals et al., 2004; Piper and Normark, 2009; Puig et al., 2014; Fisher et al., 2021). They can also function as sediment traps, accumulating large amounts of hemipelagic sediments (Carson et al., 1986; Granata et al., 1999; Liu et al., 2002; Cerrillo-Escoriza et al., 2024a).

Shelf-to-slope sediment transfer via submarine canyons is thought to be largely favored during sea-level lowstands, as fluvial systems can directly deliver sediments into canyon heads, establishing a direct link between fluvial and deep-water systems (e.g., Mitchum Jr, 1985; Vail, 1987; Posamentier and Vail, 1988; Mas et al., 2010; Khripounoff et al., 2009; 2012; Migeon et al., 2012). However, shelf-to-slope sediment transfer may also occur during highstand periods (Canals et al., 2006; Xu et al., 2008; Covault and Graham, 2010), as the transfer can also be modulated by other factors, such as the magnitude of sediment flux or the distance between the shoreline and canyon heads (Harris and Whiteway, 2011; Sweet and Blum, 2016; Puig et al., 2017; Tarrés et al., 2022). Specifically, canyon head connectivity is controlled by the margin physiography and dimensions (Sømme et al., 2009; Harris and Whiteway, 2011), as the amount of sediment transferred from coastal to deep-water environments is enhanced in steep and narrow shelves (e.g., Bernhardt and Schwanghart, 2021; Cerrillo-Escoriza et al., 2024b). Submarine canyons with high activity tend to have a direct connection to terrestrial drainage systems (Babonneau et al., 2002; Brothers et al., 2013), driving the channeling of hyperpycnal flows (e.g., Puig et al., 2017; Talling et al., 2022). This connection is particularly common in active margin settings characterized by high river discharges (Harris and Whiteway, 2011; Bernhardt and Schwanghart, 2021).

Shelf-transported sediments may alternatively be trapped in submarine canyons, depending on the strength and location of littoral cells or the occurrence of muddy depocenters (e.g., Sweet and Blum, 2016). Submarine canyons that function as sediment

traps, accumulating fine-grained sediments from major regional fluvial sources, tend to have their heads located at few kilometres from nearby shorelines (e.g., Sweet and Blum, 2016; Cerrillo-Escoriza et al., 2024a). These fine-grained sedimentary archives can be used to reconstruct past climatic, oceanographic and geological conditions (e.g., Gao and Collins, 2014; Bassetti et al., 2016; Penaud et al., 2020; Mendes et al., 2020). Furthermore, depositional signals in shallow-water muddy depocenters can be significantly altered by human activities in the river basins, including deforestation, forest fires, agriculture, mining and river damming (e.g., Boone and Worman, 2007; Gonzalez et al., 2007; Jabaloy-Sánchez et al., 2010; 2014; Mendes et al., 2012; 2015; 2020). These human-induced changes can trigger erosional regimes in the drainage basins, leading to an increased imprint of flood events in the sedimentary shelf record (e.g., Budillon et al., 2012; Mendes et al., 2020).

The Mediterranean Sea is a delta-forming environment, characterized by the frequent occurrence of small rivers that deliver high sediment yields to the coasts, while the receiving basins are subjected to weak tides and short-fetch wind waves (e.g., Anthony et al., 2014). The Mediterranean Basin also contains abundant submarine canyons, which constitute a globally distinctive population (Figure 1A; Harris and Whiteway, 2011; Amblas et al., 2018). The distinctiveness of these Mediterranean canyons stems from the fact that their genesis was influenced by a pronounced sea-level lowering and desiccation during the Late Miocene Messinian Salinity Crisis (Hsü et al., 1977; Cita et al., 1978; Harris and Whiteway, 2011; Roveri et al., 2014; Camerlenghi et al., 2020). Canyon evolution was also largely driven by erosive density flows (Bernhardt and Schwanghart, 2021). While sediment transport and depositional processes in Mediterranean submarine canyons have been widely studied (e.g., Harris and Whiteway, 2011; Harris et al., 2014; Amblas et al., 2018; Bernhardt and Schwanghart, 2021), their role in source-to-sink sedimentary processes remains poorly understood, particularly in the northern Alboran Sea. The study area, located in the northern margin of the Alboran Sea, comprises a major deltaic deposit at a regional scale, the Guadalfeo River submarine delta, which is distally and laterally associated with a series of submarine valleys including three major canyons, Motril, Carchuna, and Calahonda (Figure 1B; Cerrillo-Escoriza et al., 2023). Despite their proximity, the studied canyons exhibit distinct geomorphological and sedimentary characteristics (Cerrillo-Escoriza et al., 2024a). The shelf-incised, sinuous Motril and Calahonda canyons are located ~2 km offshore, while the straight Carchuna Canyon dissects the entire shelf (Figure 1B). Most existing research in the central sector of the northern Alboran Sea margin has focused either in inland terrestrial records (e.g., Jiménez-Moreno et al., 2013; Ramos-Román et al., 2016; 2018; García-Alix et al., 2018; Ramos-Román et al., 2018) or in deep-sea sediment cores (e.g., Jiménez-Espejo et al., 2008; Rodrigo-Gámiz et al., 2011; Ausín et al., 2015; Mesa-Fernández et al., 2022). However, the role of shelf-incised submarine canyons in sediment transfer or capture in narrow continental margins remains understudied. In this work, we present a high temporal resolution, unique Late Holocene paleoenvironmental archive recorded in the above mentioned western Mediterranean canyons. Accordingly, the aims of the present study are: (1) to reveal the different interactions between coastal sediment sources and canyon heads; (2)

to determine the impact of floods, storm events and recent human activities on canyon sedimentary infillings; (3) to investigate the coupling between shelf storage and slope sediment transfer driven by Late Holocene climatic fluctuations, by comparing our results with terrestrial and deep-water sediment records.

2 Regional setting

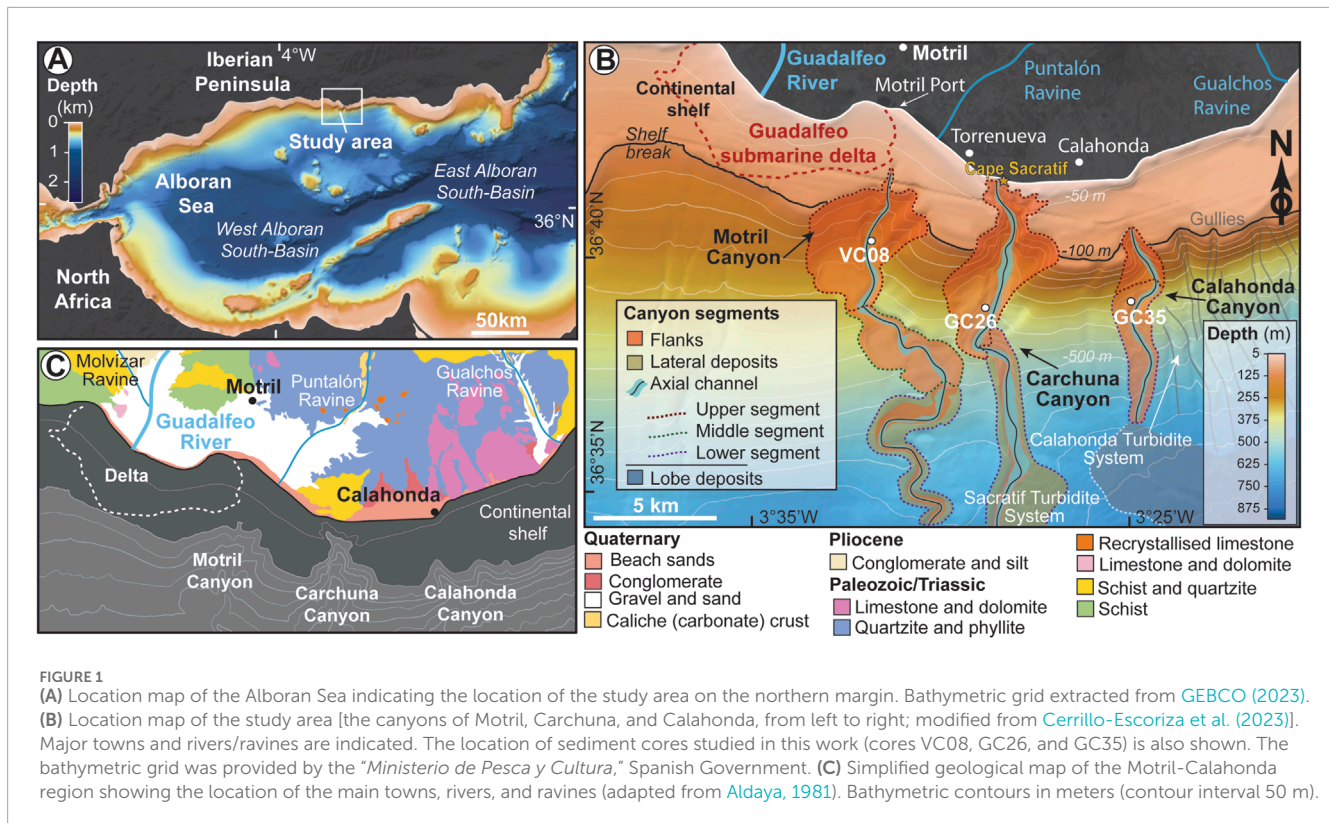
2.1 Geological setting

The Alboran Basin is a narrow, elongated basin situated in the western Mediterranean Sea (Figures 1A,B). It is regarded as a back-arc basin formed within the Betics-Rif orogenic belt, where low-angle normal fault systems contributed to crustal-scale extension. This basin developed during the early Miocene by the westward migration of the mountain belt and concomitant extension of its inner part, in a context of NW-SE convergence between the African and Eurasian plates (Comas et al., 1999; Do Couto et al., 2016). Since the Late Tortonian, the Alboran Basin underwent a tectonic inversion process due to a change in the relative motion of the African and Eurasian plates. This favored the formation of a conjugate (compressive) system of strike-slip and reverse faults, as well as folds and uplift of the basin margins (e.g., Comas et al., 1999; Platt et al., 2003; Ballesteros et al., 2008). During the Late Miocene, a significant sea-level lowering led to the desiccation of the Mediterranean Sea (i.e., the Messinian Salinity Crisis). This event exposed most of the basin margins, favoring subaerial fluvial erosion and the incision of incipient canyons that were further developed through subsequent submarine erosional processes (Frey-Martinez et al., 2004; Maillard et al., 2006; Juan et al., 2016; Gómez de la Peña et al., 2021). The regional compressive regime persisted throughout the Quaternary, resulting in differential uplift and subsidence trends along the northern basin margin (Pérez-Belzuz, 1999; Lobo et al., 2008).

The study area is located in the central sector of the northern Alboran Sea margin, in the vicinity of the Motril and Calahonda towns (Figures 1A,B). This sector off the Guadalfeo submarine delta consists of a narrow, ~3 km wide shelf deeply incised by the Motril, Carchuna and Calahonda canyons (Figure 1B). The geological basement of the Motril-Calahonda sector is composed of Paleozoic to Triassic schists, quartzites, phyllites, and limestones (Aldaya, 1981; Figure 1C).

2.2 Morpho-sedimentary setting

In the study area, the coastal sedimentary record is characterized by Late Pleistocene to Middle Holocene alluvial fans composed of conglomerates, as well as by sandy Holocene deposits comprising spit bars and infralittoral prograding wedges, formed by littoral drift and storm-driven sediment transport processes (Fernández-Salas et al., 2009; Bárcenas et al., 2011; Ortega-Sánchez et al., 2014). The Carchuna infralittoral prograding wedge consists of coarse-grained sediments and is laterally bounded by the Carchuna Canyon head (Figure 1B; Fernández-Salas et al., 2009; Ortega-Sánchez et al., 2014).



Fluvial supply is largely provided by the Guadalfeo River, a major regional fluvial system (Figures 1B,C) that has formed a submarine prodeltaic system west of the Motril Canyon head (Figure 1B; Jabaloy-Sánchez et al., 2014; Lobo et al., 2015). In addition, two small streams with torrential discharges during the rainy season (Puntalón and Gualchos ravines; Figure 1B) also provide sediments to coastal and shallow-water environments. These small ravines are short (<20 km), occur in small basins (<120 km²), and have steep slopes (>3.6°) (Bárcenas et al., 2011).

Deep-water depositional systems in the study area comprise the Sacratif Turbidite System, which includes the Motril and Carchuna canyons, and the Calahonda Turbidite System (Cerrillo-Escoriza et al., 2023; 2024a) (Figure 1B). The Motril Canyon, located 3 km south-east of the Guadalfeo River mouth, displays a sinuous morphology across the slope (Figure 1B). The straight Carchuna Canyon crosses the entire shelf and is located 200 m off Cape Sacratif (Figure 1B). Both canyon systems terminate in large sedimentary lobes fed by distributary channels (Pérez-Belzuz and Alonso, 2000; Pérez-Belzuz et al., 2000) with superimposed sediment wave fields (Muñoz et al., 2017; Cerrillo-Escoriza et al., 2024b). The Calahonda Canyon, located 2.5 km south of Calahonda town, exhibits a sinuous valley across the slope, and together with several gullies eroding the slope, have formed a sedimentary lobe fed by distributary channels (Figure 1B) (Ercilla et al., 2019).

2.3 Oceanographic regime

The northern Alboran Sea is a microtidal, low-energy wave environment (e.g., Parrilla and Kinder, 1987). Easterly winds are

more frequent than westerly winds, although waves from the west-southwest are slightly more energetic (e.g., Jabaloy-Sánchez et al., 2014). Littoral drift shows substantial variability due to the coastal morphology and meteorological conditions (e.g., Stanley et al., 1975; Bárcenas, 2013). On the shelf, currents show alternating directions in response to changes in wind dominance (Bárcenas et al., 2011). Surficial current patterns are influenced by the entrance of Atlantic waters through the Strait of Gibraltar that circulates eastward at water depths of 150–250 m (Brankart and Pinardi, 2001; Millot, 2009; 2014). They form the so-called Atlantic Jet, which feeds two anticyclonic gyres (Western and Eastern Alboran Gyres) (García-Lafuente et al., 1998; Renault et al., 2012).

The coast in the study area is affected by wave trains coming from W, WSW, SW, ESE and E, oblique to the main E-W coastal trend (Ortega-Sánchez et al., 2014). In particular, the shelf around the Carchuna Canyon head (Figure 1B) exacerbates coastal swell and storm-related processes, leading to increased nearshore wave heights, mostly from westerly waves. This, in turn, triggers long-term coastal erosion due to the concentration of wave energy (Ortega-Sánchez et al., 2014). Additionally, a distinct downcanyon bottom flow with velocities ranging between 20 and 30 cm·s⁻¹ has been observed within the Carchuna Canyon (Serrano et al., 2020).

3 Materials and methods

This study is based on a multi-proxy analysis of three sediment cores (ALS19_VC08, ALS19_GC26, and ALS19_GC35; hereafter VC08, GC26, and GC35; Figure 1B) collected on board the RV

Sarmiento de Gamboa during the ALSSOMAR oceanographic expedition in 2019. The cores were retrieved using vibro corer (VC) and gravity corer (GC) devices. Core VC08 is 401 cm long and was collected at 297 m water depth at 36°40.3774'N, 3°31.821'W; core GC26 is 213 cm long and was obtained at 407 m water depth at 36°038.989'N, 3°028.815'W; and core GC35 is 243 cm long and was collected at 402.12 m water depth at 36°39.1411'N, 3°024.7561'W. Onboard, the cores were cut into 1-m sections and refrigerated. They were analyzed at the University of Vigo (Spain) using a computed tomography (CT) scanner and then split lengthwise into two halves (working and archive). Visual core descriptions and non-destructive sedimentary analyses, such as X-ray fluorescence (XRF) scanning, were subsequently performed on the archive halves. After core scanning analyses, both the archive and working halves were transported for permanent storage at 3°C at the core repository of the *Instituto Andaluz de Ciencias de la Tierra*, IACT-CSIC (Spain). The working halves were subsequently sampled for radiocarbon (^{14}C) dating, as well as for sedimentological and mineralogical analyses (see below; [Supplementary Tables S1–S3](#)).

3.1 Core chronology

A total of eighteen accelerator mass spectrometry (AMS) radiocarbon (^{14}C) dates were obtained for the chronology of cores VC08, GC26, and GC35 ([Table 1](#)). The age-depth model of core VC08 is based on eight AMS ^{14}C radiocarbon dates of mixed benthic foraminifera, a piece of wood and mixed bivalve shells (six, one and one sample, respectively). The age-depth models of cores GC26 and GC35 are based on four and six AMS ^{14}C dates of mixed benthic foraminifera, respectively. AMS ^{14}C dating of benthic foraminifera was performed at the Laboratory of Ion Beam Physics at ETH Zürich (Switzerland), while a piece of wood and mixed bivalve shell samples were dated by Beta Analytic Carbon Dating Service (USA). At ETH Zürich, ^{14}C measurements can be performed on carbonate samples containing only 0.3–1 mg carbonate. To ensure accuracy, samples were first leached with 100 mL of 0.02 M HCl for cleaning to remove any surface contamination of the carbonates ([Bard et al., 2015](#)), before being decomposed in 85% phosphoric acid in septa-sealed vials ([Wacker et al., 2013a](#)). The resulting CO_2 was measured directly using an accelerator mass spectrometer ([Wacker et al., 2010](#)), equipped with a gas ion source ([Wacker et al., 2013b](#)) – i.e., no graphitisation step is required. All ^{14}C ages were calibrated using the CALIB Radiocarbon Calibration Program 8.2 ([Stuiver et al., 2021](#)). The MARINE20 calibration curve ([Heaton et al., 2020](#)) and the INTCAL20 calibration curve ([Reimer et al., 2020](#)) were used to convert ^{14}C ages to calendar ages with 2σ precision ([Table 1](#)). As proposed for this region in previous studies [[Reimer and McCormac \(2002\)](#) after [Siani et al. \(2000\)](#)] and based on the Marine Reservoir Correction Database ([Reimer and Reimer, 2001](#)), we applied a local marine reservoir age correction (ΔR) of -28 ± 35 years to all the marine samples ([Table 1](#)).

A linear interpolation based on ^{14}C ages ([Table 1](#)) was used to produce age-depth models ([Figure 2](#)), assuming constant and linear sediment accumulation rates between dated levels. Zero validation was applied, i.e., projecting the regression line of the uppermost ^{14}C dating to the core tops. The core top was considered recent (i.e.,

the time of sediment coring at 2019 CE; see [Figure 10](#) in [Cerrillo-Escoriza et al., 2024a](#)). For years given with the notation BP (Before Present), the zero age is 1950 CE (Current Era). Moreover, we used Gregorian calendar years (BCE/CE; Before Current Era/Current Era) for historical ages.

3.2 Sedimentological analysis

Sediment characterization was aided by means of visual core descriptions and sediment composition analysis. Sediment characterization included lithology, sediment texture and structure, sediment color using the Munsell color chart, bioturbation intensity and grain size.

Macroscopic visual core observations were performed using (a) high-resolution line scan digital images obtained from archive halves using an ITRAX X-ray fluorescence (XRF) core scanner at the Center for Scientific and Technological Support to Research (CACTI) of the University of Vigo (Spain), and (b) X-ray computed tomography (CT) images obtained from archive halves using a HITACHI ECLOS 16 Multislice CT scanner at the Veterinary Teaching Hospital Rof Codina in Lugo (Spain). Details on CT acquisition can be found in [Mena et al. \(2015\)](#). The resulting CT images (~1800 images per section) were imported into the image editing software FIJI (ImageJ 2.16.0; [Rueden et al., 2017](#)), which allows the virtual extraction of longitudinal, transverse and oblique sections. Mean Hounsfield unit (HU) values were also extracted from the CT images to calculate sediment density using the following equation: density (g/cm^3) = $8 \times 10^{-4} \times \text{HU} + 1$ ([Reilly et al., 2017](#)). CT images were visually examined to identify fine-scale stratigraphic changes and sedimentary structures in a non-destructive way (e.g., [Van Daele et al., 2014](#); [Fouinat et al., 2017](#); [Salabarnada et al., 2018](#); [López-Quirós et al., 2024](#)).

Bulk grain-size distributions were measured in cores VC08, GC26, and GC35 using a COULTER® LS 13 320 Laser Diffraction Particle Size Analyzer at the University of Vigo (Spain). Each analysis was performed on ~10 g of bulk sediment material collected every 5 cm ([Supplementary Tables S1–S3](#)), providing the grain size spectra between 0.4 and 2000 μm (clay to sand). The geometric mean, skewness, kurtosis, and sorting were calculated using the GRADISTAT 9.0 software ([Blott and Pye, 2001](#)) following the method of [Folk and Ward \(1957\)](#). In addition, the relative composition of terrigenous and biogenic grains, grain size and shape were microscopically examined every 25 cm and in selected levels ([Supplementary Tables S1–S3](#)). The selected sampling levels were chosen based on major sedimentological changes observed during macroscopic (visual) core descriptions and analysis of downcore elemental concentrations. Samples were washed with tap water through a sieve of 63 μm diameter and then dried in an oven at 40°C. The sand-sized fraction (>63 μm) was analyzed under a trinocular stereo microscope (StereoBlue EVO). Several images were taken with a CMEX camera connected to the stereo microscope and captured with the ImageFocus software. For further investigation on grain composition, X-ray powder diffraction (XRPD) was performed on the same low-resolution sampling levels ([Supplementary Tables S1–S3](#)) to determine the average bulk (mineral) composition. For XRPD determinations,

TABLE 1 Radiocarbon dates from sediment cores VC08, GC26 and GC35. The CALIB 8.1.0 software (Stuiver et al., 2021) and the MARINE20 dataset (Heaton et al., 2020) were used to convert the ¹⁴C ages to calendar ages with 2σ precision, applying a local marine reservoir age correction (ΔR) of -28 ± 35 years following Reimer and McCormac (2002) after Siani et al. (2000). The calibrated age of wood was calculated by using the INTCAL20 calibration curve (Reimer et al., 2020). (*) Radiocarbon dates not used in the age model, considered to be redeposited and/or reworked from transported older sediments. (#) Dates out of range for the calibration curve Marine20. Tentative calibration is adjusted for this work after 95.4% probability. All measured ETH samples, except ETH nr.126776.3.2, were leached. Note that the numbers in bold are the radiocarbon dates shown in the stratigraphic log of sediment cores VC-08, GC-26, and GC-35, which are presented in Figures 3, 6, 7.

Core depth (cm)	Lab ID	Material	Uncorrected age (¹⁴ C-yr BP)	Error (±yr)	Corrected and calibrated age (2σ) (cal. yr BP)		Calibrated age (2σ) (BCE/CE)	
					Lower cal. range	Upper cal. range	Median probability	Median probability
ALS19-VC-08								
40	ETH nr. 130578.1.1	Mixed benthic foraminifera	610	60	0	264	114	1836 CE
64	Beta - 621229	A piece of wood	530	30	511	556	539	1411 CE
100 (*)	ETH nr. 126785.1.1	Mixed benthic foraminifera	13185	100	14652	15421	15053	13104 BCE
150	ETH nr. 130579.1.1	Mixed benthic foraminifera	905	60	200	542	385	1565 CE
200	ETH nr. 130580.1.1	Mixed benthic foraminifera	1520	60	735	1131	936	1014 CE
300	ETH nr. 130581.1.1	Mixed benthic foraminifera	1595	60	820	1220	1016	934 CE
380	Beta - 621230	Mixed bivalve shells	2074	46	1333	1692	1504	446 CE
395	ETH nr. 130582.1.1	Mixed benthic foraminifera	2505	60	1814	2276	2025	76 BCE
ALS19-GC-26								
36 (#)	ETH nr. 130572.1.1	Mixed benthic foraminifera	430	80	0	217	<100	<1850 CE
90	ETH nr. 130573.1.1	Mixed benthic foraminifera	875	80	134	537	358	1565 CE
135	ETH nr. 130574.1.1	Mixed benthic foraminifera	615	60	0	267	117	1833 CE
176	ETH nr. 130575.1.1	Mixed benthic foraminifera	985	60	288	616	454	1494 CE

(Continued on the following page)

TABLE 1 (Continued) Radiocarbon dates from sediment cores VC08, GC26 and GC35. The CALIB 8.1.0 software (Stuiver et al., 2021) and the MARINE20 dataset (Heaton et al., 2020) were used to convert the ¹⁴C ages to calendar ages with 2σ precision, applying a local marine reservoir age correction (ΔR) of -28 ± 35 years following Reimer and McCormac (2002) after Siani et al. (2000). The calibrated age of wood was calculated by using the INTCAL20 calibration curve (Reimer et al., 2020). (*) Radiocarbon dates not used in the age model, considered to be redeposited and/or reworked from transported older sediments. (#) Dates out of range for the calibration curve Marine20. Tentative calibration is adjusted for this work after 95.4% probability. All measured ETH samples, except ETH nr.126776.3.2, were leached. Note that the numbers in bold are the radiocarbon dates shown in the stratigraphic log of sediment cores VC-08, GC-26, and GC-35, which are presented in Figures 3, 6, 7.

Core depth (cm)	Lab ID	Material	Uncorrected age (¹⁴ C yr BP)	Error (±yr)	Corrected and calibrated age (2σ) (cal. yr BP)		Calibrated age (2σ) (BCE/CE)	
					Lower cal. range	Upper cal. range	Median probability	Median probability
ALS19-GC-35								
45 (#)	ETH nr. 141574.1.1	Mixed benthic foraminifera	260	60	0	124	<70	<1880 CE
80	ETH nr. 126775.1.1	Mixed benthic foraminifera	730	100	0	422	217	1733 CE
95	ETH nr. 141575.1.1	Mixed benthic foraminifera	645	60	0	290	139	1811 CE
140	ETH nr. 141577.1.1	Mixed benthic foraminifera	1715	60	944	1302	1138	812 CE
170	ETH nr. 126776.3.2	Mixed benthic foraminifera	3115	100	2466	3082	2783	834 BCE
235	ETH nr. 126777.1.1	Mixed benthic foraminifera	5865	100	5857	6378	6110	4161 BCE

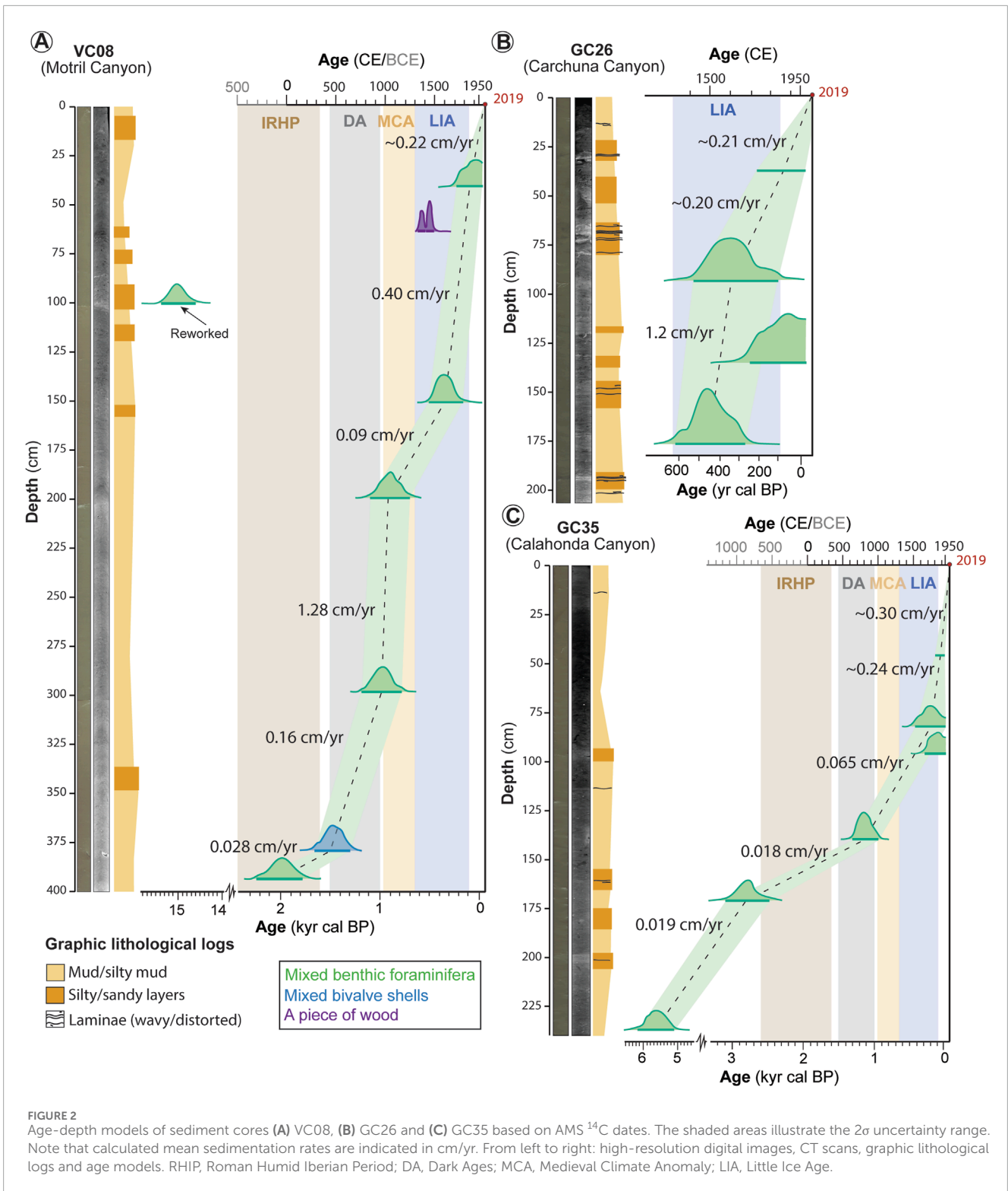


FIGURE 2 Age-depth models of sediment cores (A) VC08, (B) GC26 and (C) GC35 based on AMS ¹⁴C dates. The shaded areas illustrate the 2σ uncertainty range. Note that calculated mean sedimentation rates are indicated in cm/yr. From left to right: high-resolution digital images, CT scans, graphic lithological logs and age models. RHIP, Roman Humid Iberian Period; DA, Dark Ages; MCA, Medieval Climate Anomaly; LIA, Little Ice Age.

selected sediment samples were hand ground using an agate mortar, and then analyzed with a PANalytical X’Pert Pro diffractometer (CuKα radiation, 45 kV, 40 mA) equipped with a RTMS X’Celerator solid-state detector (*Instituto Andaluz de Ciencias de la Tierra, IACT-CSIC, Spain*). Samples were scanned in the 2θ range from 3° to 69.9°, with a step size of 0.0084° (2θ)/s. The counting time was

set at 11 min per sample. Diffraction data were analyzed using the HighScore software.

Carbonate (CaCO₃) content was also measured in core VC08 and compared against XRF core scanner data (see below). Sediment samples were collected at 10 cm intervals ([Supplementary Table S1](#)), with macroscopic shells removed to ensure representative carbonate

values. Samples were freeze-dried for 2–3 days at the Department of Stratigraphy and Paleontology of the University of Granada (Spain), and then hand-ground to a homogeneous powder using an agate mortar. The initial sample dry weight was recorded before carbonate dissolution. To determine the carbonate content, the samples were treated with 1M hydrochloric acid (HCl) until the reaction ceased. The acid-treated samples were left to stand for 24 h and subsequently washed with deionized H₂O via centrifugation for multiple cycles at 2500 rpm to remove any residual acid. Samples were then freeze-dried and reweighed, with weight loss used to calculate sediment CaCO₃ content.

3.3 Geochemical and physical analysis

Downcore elemental concentrations were measured on core surfaces of the archive halves at 5-mm interval resolution using an ITRAX X-ray fluorescence (XRF) core scanner equipped with a molybdenum X-ray tube at the CACTI (University of Vigo, Spain). Core sections were scanned using a voltage of 30 kV, a current of 55 mA and an exposure time of 20 s. XRF spectral data were processed using Q-spec 8.6.0 spectral analysis software, which applied a standard fitting procedure to the original spectra (Croudace et al., 2006). The results of the XRF scanning are provided as element intensities in total counts per second (cps), which are relative to the real chemical concentration of the measured elements (e.g., Weltje and Tjallingii, 2008). Magnetic susceptibility (MS) was measured at 1-cm interval resolution using a Bartington MS3 fitted within the ITRAX core scanner. The measured MS is a volume magnetic susceptibility (χ) with units of 10⁻⁵ SI. For this study, besides MS, we report the following elements and elemental ratios: silica (Si), potassium (K), titanium (Ti), aluminum (Al), iron (Fe), bromine (Br), and calcium (Ca), as well as the Rb/Zr, Br/Ti, Fe/Ca, Ti/Ca, and Sr/Ca ratios. Additionally, measurements of molybdenum (Mo) incoherent and coherent scattering (inc/coh) were reported.

Elemental counts of Si, K, Ti, and Al, frequently used as proxies for variations in terrigenous sediment input (e.g., Rothwell and Croudace, 2015; Salabarnada et al., 2018; Evangelinos et al., 2020; López-Quirós et al., 2021; 2024), have been plotted against lithological logs to assess variations in terrigenous sediment supply (Figure 1B). Those elements are considered to be indicative of variations in precipitation and/or runoff. For example, Ti is mostly found in minerals associated with sand and silt; K is a major component of clay minerals such as illite or in K-feldspar, and is mainly transported to marine environments by riverine runoff. Similarly, elemental counts of Fe have been used as tracers of terrestrial detrital input (Rothwell and Croudace, 2015). Elemental counts of Ca and strontium (Sr) have been frequently used as indicators of marine biogenic material as they reflect the biogenic carbonate sediment content (Zaragosi et al., 2006; Rothwell and Croudace, 2015). Elemental counts of Br are reported as sensitive indicators of organic matter in sediments and of paleoproductivity (Ziegler et al., 2008; Ziegler et al., 2010; Caley et al., 2011). The distribution of terrigenous and biogenic elements is expected to show anti-correlative patterns (e.g., Rothwell and Croudace, 2015; Mendes et al., 2020; López-Quirós et al., 2021; 2024).

Rb/Zr ratios are sensitive to grain-size variations within the terrigenous fraction, as Rb resides mainly in clay minerals and Zr in coarser grains (Salabarnada et al., 2018; Mendes et al., 2020). Fe/Ca and Ti/Ca ratios have been largely reported as tracers of terrigenous vs biogenic CaCO₃ and/or of riverine input (e.g., Dickson et al., 2010; Steinke et al., 2014; Liu et al., 2016; Mendes et al., 2020; Mesa-Fernández et al., 2022). In the Alboran Sea, Ti/Ca ratios have also been attributed to tracers of Saharan eolian dust input *versus* productivity (e.g., Bouimtarhan et al., 2013; López-González et al., 2019). In contrast, Mesa-Fernández et al. (2022) recently argued that Ti/Ca ratios are not reliable eolian proxies for the Alboran Sea, as the eolian input does not control the relative variations between terrigenous and carbonate inputs in the western Mediterranean Basin. Additionally, more specific interpretations concerning terrigenous input *versus* productivity have been used. For instance, Br/Ti ratios are used as indicators of organic matter in sediments and of paleoproductivity (e.g., Bahr et al., 2014; Salabarnada et al., 2018; Evangelinos et al., 2020; López-Quirós et al., 2021). Sr/Ca ratios have been used to distinguish between biogenic and detrital carbonate, as Ca can be supplied from both biogenic precipitation and from terrigenous sources such as feldspars and clay minerals. Therefore, co-variation of Ca and Sr is likely to indicate that Ca is mainly derived from biogenic precipitation (e.g., Hillaire-Marcel and De Vernal, 2007). In addition, Sr/Ca ratios have been used as tracers of aragonite, as Sr is favorably incorporated into aragonite, and are hence potentially useful in distinguishing foraminiferal calcite from bivalve and/or gastropod aragonite (e.g., Rothwell et al., 2006; Thomson et al., 2006; Hodell et al., 2008; Grove et al., 2010).

Mo (inc/coh) ratio has been used as indicator of organic matter content in sediments (e.g., Sáez et al., 2009; Chawchai et al., 2016; López-Quirós et al., 2024). The Mo inc/coh scattering ratio depends on the average atomic number of the materials in the sediment. For example, organic carbon has a lower average atomic number than silica, aluminosilicate and carbonate minerals.

3.4 Basis for sediment unit distinction

Sedimentary units were defined by integrating visual core descriptions with major variations in downcore physical properties (magnetic susceptibility and density) and geochemical composition (XRF). To strengthen the correlation between these visual core characteristics/physical properties and the geochemical signature of the sediments, a principal component analysis (PCA) was applied to the XRF datasets (Supplementary Figure S1). Data standardization by subtracting the mean and dividing by the standard deviation was performed before PCA analyses. PCA analyses of the XRF dataset reduced the dimensionality of the data scatter and variability to principal components (e.g., Evangelinos et al., 2020). The PCA analyses, performed using a correlation matrix in PAST-PALaeontological STATistics 4.03 software (Hammer et al., 2001), enhanced the identification of distinct sedimentary units based on the combined variability in sedimentological/physical and geochemical characteristics.

After integration with our ¹⁴C results, these sedimentary units broadly coincide with the last four historical climatic periods

described by Moreno et al. (2012) over the past 2000 years (Supplementary Figure S1). Consequently, the units defined here do not strictly correspond to conventional lithological units, which are based primarily on visual core features, nor to sedimentary facies, which are linked to specific depositional environments (Tucker, 2001). Instead, they represent an integrated classification based on downcore proxy relationships, correlation matrices and chronological markers that record intervals of significant climatic and environmental change through time.

4 Results

4.1 Age model and sedimentation rates

A ^{14}C date of ca. 2025 cal. yr BP (76 BCE) obtained at the base of core VC08 (Motril Canyon) indicates that this core records the entire Common Era (Table 1), covering the last four historical climatic periods: the Little Ice Age (LIA), the Medieval Climate Anomaly (MCA), the Dark Ages (DA), and the Roman Humid Iberian Period (RHIP) (Moreno et al., 2012). Two periods of high sedimentation rate occurred: from ca. 1016 to ca. 936 cal. yr BP (934–1014 CE) with a rate of 1.28 cm/yr, and from ca. 385 cal. yr BP (1565 CE) to Recent times, ranging from 0.44 to 0.22 cm/yr (Figure 2A). At VC08, however, and based on interpreted sediment features (see Section 5), we consider the ^{14}C date of ca. 15053 cal. yr BP obtained at 100 cm depth (Figure 2A; Table 1) to be unreliable, as the sediment interval is likely to have been redeposited and/or reworked. In addition, the ^{14}C date obtained at 64 cm depth using a piece of wood (1411 CE) appears anomalously old compared to the foraminifer-based dates from the intervals above (1836 CE) and below (1565 CE) (Figure 2A; Table 1). This reversal age may be due to the well-known “old wood” effect (Bowman, 1990; Kim et al., 2019).

Core GC26 (Carchuna Canyon) covers the period from ca. 454 cal. yr BP (1494 CE) onwards and shows consistently high sedimentation rates (Figure 2B; Table 1). The highest rate, 1.2 cm/yr, occurred from ca. 454 to ca. 358 cal. yr BP (1494–1565 CE), followed by relatively high, stable rates of ~ 0.20 cm/yr, persisting to Recent times (Figure 2B). At GC26, however, an age offset is observed between the ^{14}C dates obtained at 135 cm depth (117 CE) and 90 cm depth (358 CE) (Figure 2B; Table 1). Given the stratigraphic position of these intervals, the presence of younger carbon at depth in the sedimentary column cannot be explained by redeposition or sediment reworking. Based on the interpreted sediment features (see Section 5), the most plausible explanation is related to the effect of bioturbation, whereby younger carbon was introduced into deeper layers, locally altering the age–depth model (e.g., Boudreau, 1998).

A ^{14}C date of ca. 6110 cal. yr BP (4161 BCE) obtained at the base of core GC35 (Calahonda Canyon) indicates that this core covers from the mid-Holocene to Recent times (Table 1). Low sedimentation rates (0.018–0.065 cm/yr) were recorded from ca. 6110 to ca. 217 cal. yr BP (4161 BCE – 1733 CE). However, a period of increased sedimentation rate (0.24–0.30 cm/yr) occurred from ca. 217 cal. yr BP (1733 CE) to Recent times (Figure 2C). Similarly to core GC26, an age offset is observed in GC35 between the ^{14}C dates at 95 cm depth (1811 CE) and 80 cm depth (1733 CE) (Figure 2C; Table 1), likely due to bioturbation mixing depth (e.g., Boudreau, 1998).

4.2 Sedimentological and geochemical records

4.2.1 Motril Canyon

Sedimentological and geochemical analyses of VC08 revealed five distinct units (Units V to I, from bottom to top; Figure 3) corresponding to the last four historical climate periods and/or transitions up to Recent times (Moreno et al., 2012): RHIP, DA, MCA, and LIA (Figures 2A, 3).

The lowermost Unit V (400–325 cm below sea floor, bsf) covers almost the entire RHIP (from ca. 2025 to 1504 cal yr BP, i.e., from 76 BCE to 446 CE) and likely the lower DA (Figure 3). This unit is composed of brownish light green mud and silty mud, with subtle variations of the coarse and fine fractions, showing an upward coarsening trend, with no primary sedimentary structures (Figure 3). An increase of the sand fraction is observed at the upper part of the unit (348–335 cm bsf) (Figure 3). Sediments in Unit V are poorly to very poorly sorted, and consist largely of terrigenous components, including sub-angular grains of quartz and K-feldspar, plagioclase and muscovite. Also, bioclasts, primarily benthic foraminiferal and mollusk (bivalve/gastropods) shells, as well as mottling indicative of bioturbation, were observed throughout the unit (Figures 3, 4A,B). Terrigenous elements (Si, K, Al, Ti, and Fe) display an overall upward decreasing trend up to 377 cm bsf, followed by a prominent, fluctuating upward increasing trend towards the top unit (Figure 3). In contrast, Ca exhibits an overall upward increasing trend up to 350 cm bsf, followed by a decreasing trend towards the top unit. Notably, two major fluctuations at around 349 and 336 cm bsf coincide with low values in terrigenous elements and Ca (Figure 3). Fe/Ca and Ti/Ca ratios follow similar trends than terrigenous elements. However, where terrigenous elements exhibit low values, Fe/Ca and Ti/Ca ratios show high values (Figure 3). In contrast, Br and Br/Ti ratios, as well as Mo (inc/coh) ratio display anticorrelated trends with terrigenous elements (Figure 3). Besides, Sr/Ca ratio displays no significant variability apart from notable peaks that also correlate with peaks in Fe/Ca, Ti/Ca and Br/Ti ratios (Figure 3).

Unit IV (325–265 cm bsf) spans the upper DA, including the DA-MCA transition, which occurred before ca. 1014 cal yr BP (i.e., before 934 CE; Figures 2A, 3). This unit is composed of brownish light green mud/silty mud, with a homogeneous composition of the coarse and fine fractions. Unit IV contains slightly lower sand contents than Unit V (Figure 3). Unit IV has a mottled appearance indicative of bioturbation and lacks primary sedimentary structures (Figure 3). Sediments in this unit are poorly sorted and are mainly composed of terrigenous components such as quartz and K-feldspar grains, plagioclase and mica. Bioclastic elements, including foraminiferal and mollusk shells, are also present. In contrast, this unit displays higher abundances of foraminiferal and mollusk shells than Unit V. Terrigenous elements (Si, K, Al, Ti, and Fe) and Rb/Zr, Fe/Ca, and Ti/Ca ratios, as well as Mo (inc/coh) ratio exhibit upward increasing trends with moderate to high fluctuations. In contrast, Ca, Br, and Br/Ti ratios display weak anticorrelated trends with terrigenous elements and Fe/Ca and Ti/Ca ratios. Sr/Ca ratio exhibits no significant variability, except for some subtle peaks that correlate with peaks in Fe/Ca, Ti/Ca, and Br/Ti ratios (Figure 3).

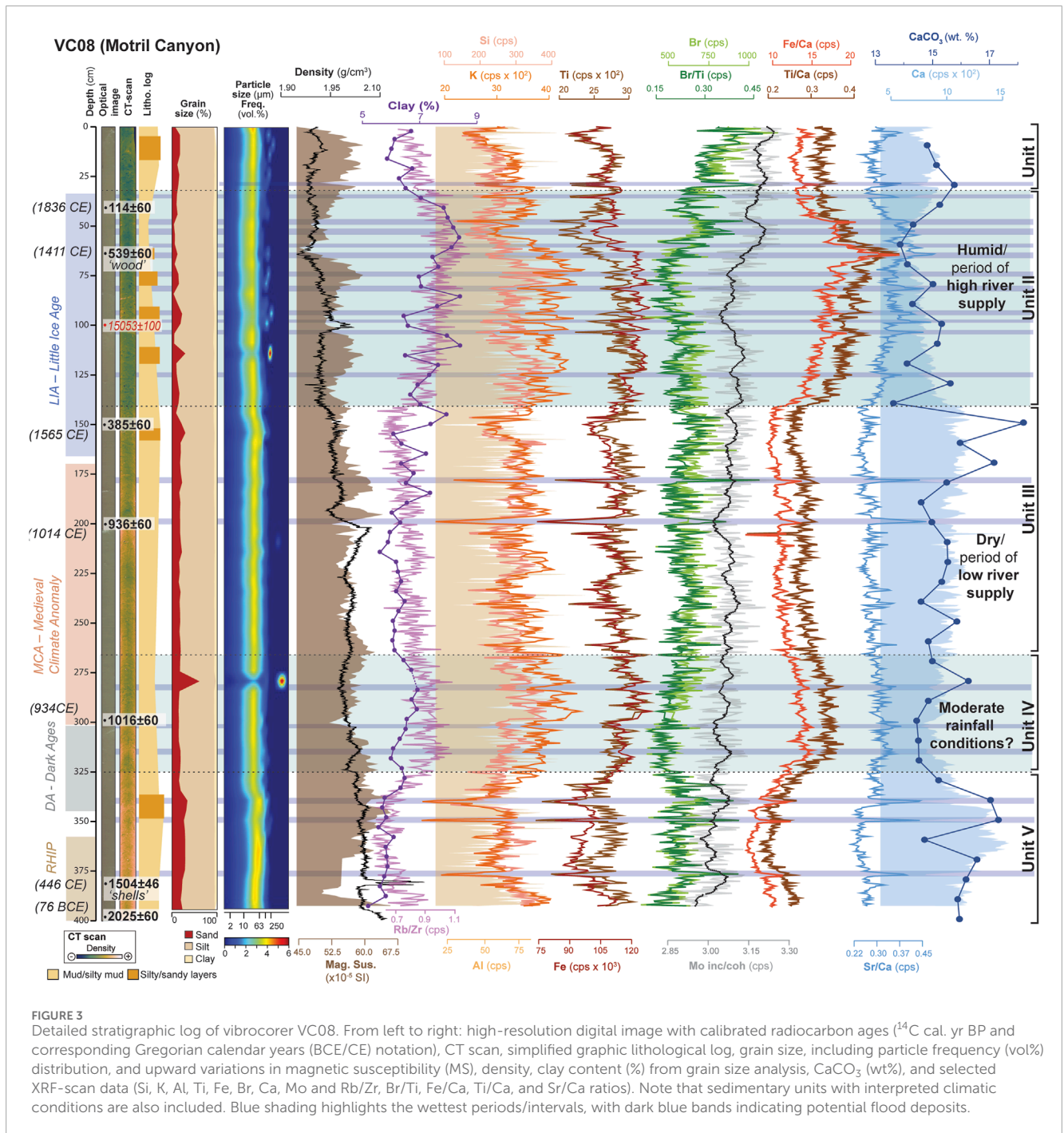


FIGURE 3 Detailed stratigraphic log of vibrocorer VC08. From left to right: high-resolution digital image with calibrated radiocarbon ages (¹⁴C cal. yr BP and corresponding Gregorian calendar years (BCE/CE) notation), CT scan, simplified graphic lithological log, grain size, including particle frequency (vol%) distribution, and upward variations in magnetic susceptibility (MS), density, clay content (%) from grain size analysis, CaCO₂ (wt%), and selected XRF-scan data (Si, K, Al, Ti, Fe, Br, Ca, Mo and Rb/Zr, Br/Ti, Fe/Ca, Ti/Ca, and Sr/Ca ratios). Note that sedimentary units with interpreted climatic conditions are also included. Blue shading highlights the wettest periods/intervals, with dark blue bands indicating potential flood deposits.

Unit III (265–140 cm bsf) spans the entire MCA, including the MCA-LIA transition, which occurred before ca. 385 cal yr BP (i.e., before 1565 CE; Figures 2A, 3). This unit consists of brownish light green mud and silty mud, characterized by a weak upward coarsening trend (Figure 3). However, a significant increase of the sand fraction was observed in the upper part of the unit from 158 to 150 cm bsf (Figure 3). Sediments within unit III are poorly sorted, composed largely of terrigenous components such as quartz, K-feldspar, plagioclase, and mica grains. Bioclastic elements, including foraminiferal and mollusk shells, are also present. Unit III also has a mottled appearance indicative of bioturbation

and lacks primary sedimentary structures (Figure 3). Terrigenous elements such as Si, K, Al, Ti, and Fe display very weak upward decreasing trends with moderate fluctuations, although the values are lower than the underlying Unit IV (Figure 3). In contrast, Ca displays no significant upward variability but shows higher values than the underlying sediments (Figure 3). Likewise, Mo (inc/coh) ratio, despite exhibiting minor fluctuations, displays no significant variability (Figure 3). Fe/Ca and Ti/Ca ratios display comparable trends to terrigenous elements. However, when terrigenous elements exhibit low values, Fe/Ca and Ti/Ca ratios show correspondingly high values (Figure 3). In contrast, Br and Br/Ti ratio display

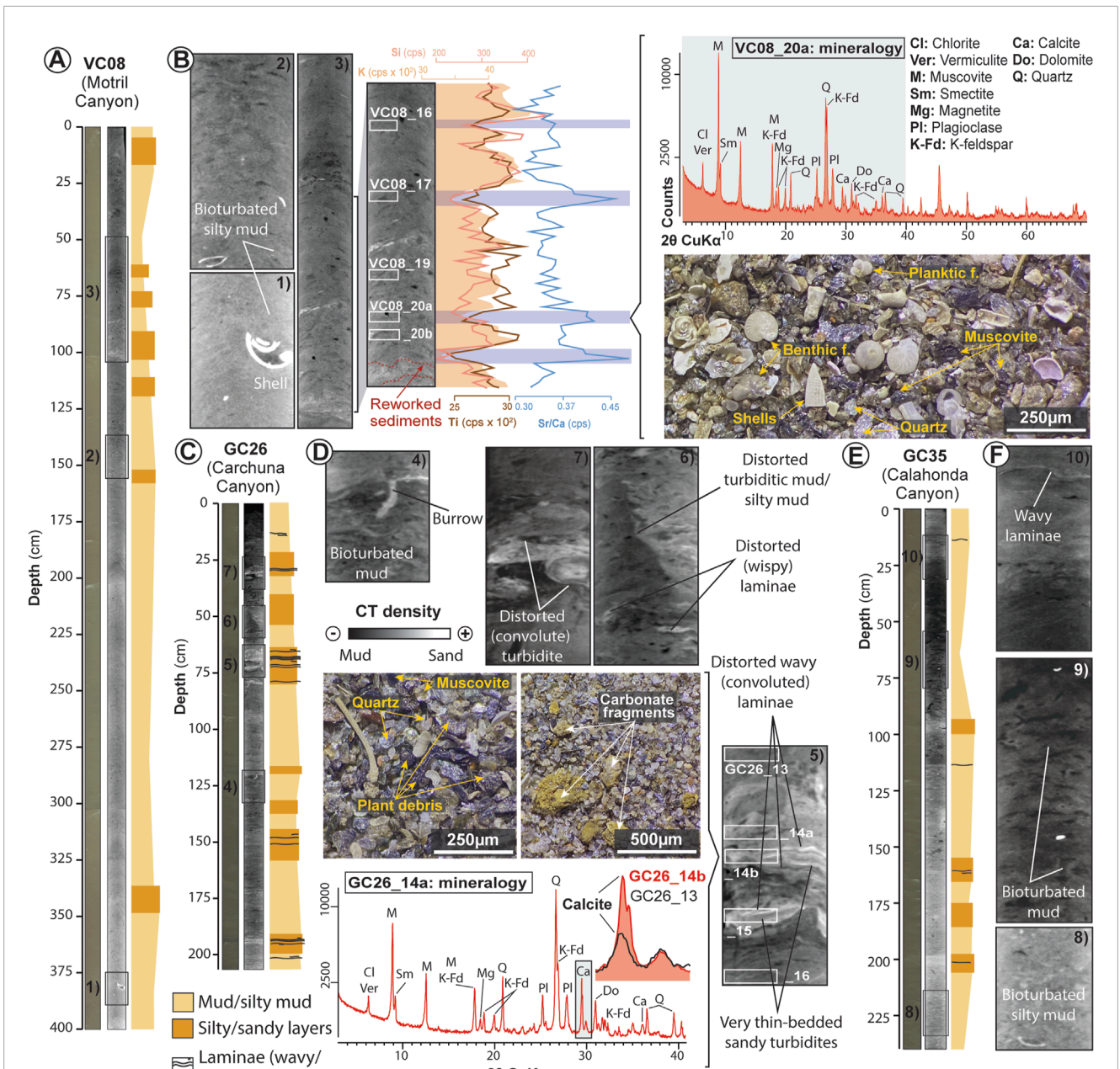


FIGURE 4 Simplified graphic lithological logs accompanied by detailed sedimentological observations at the studied sediment cores VC08 (Motril Canyon), GC26 (Carchuna Canyon) and GC35 (Calahonda Canyon). **(A)** Graphic log of VC08 including high-resolution digital image of the core and its CT scan. The squared areas (1, 2, and 3) correspond to enlarged CT scan images displaying detailed sedimentological features (grouped in B). **(B)** Enlarged views of the marked areas in (A) showing the mottled appearance indicative of bioturbation and absence of primary sedimentary structures (B-1, B-2, and B-3). An additional enlarged area from B-3 is included, along with selected XRF-scan data and the stratigraphic sample position. A representative X-ray diffraction pattern of bulk sediments from a selected sample (VC08_20a) and the corresponding photomicrograph of the coarse fraction (>63 μm) are also included. Sediment intervals interpreted as flood deposits are highlighted in blue. **(C)** Graphic log of GC26 including high-resolution digital image of the core and its CT scan. The squared areas (4, 5, 6, and 7) correspond to enlarged CT scan images displaying detailed sedimentological features (grouped in D). **(D)** Enlarged views of the marked areas in C displaying bioturbation (D-4) and sedimentary structures such as convoluted and wavy laminae (D-5, D-6, and D-7). Enlarged picture in D-7 also includes stratigraphic sample position, with an example of a characteristic X-ray diffraction pattern of bulk sediments from a selected sample (GC26_14a) and the corresponding photomicrograph of the coarse fraction (>63 μm). These samples correspond to intervals interpreted as thin-bedded sandy turbidites. For comparison, the (104) diffraction peak of calcite from sample GC26_13 is superimposed on the GC26_14a pattern. **(E)** Graphic log of GC35 including high-resolution digital image of the core and its CT scan, with squared areas (8, 9, 6, and 10) corresponding to enlarged CT scan images displaying detailed sedimentological features (grouped in F). **(F)** Enlarged views of the marked areas in E showing a mottled appearance indicative of bioturbation and sedimentary structures such as wavy laminae (F-8, F-9, and F-10).

anticorrelated trends with terrigenous elements (Figure 3). Besides, Sr/Ca ratio displays no significant variability apart from some peaks which also correspond to peaks in Fe/Ca, Ti/Ca, and Br/Ti ratios (Figure 3).

Unit II (140–33 cm bsf) covers the entire LIA (from ca. 385 to 114 cal yr BP, i.e., from 1565 to 1836 CE; Figures 2A, 3). Unit II, composed of brownish light green mud/silty mud, exhibits a weak fining-upward trend, with interbedded sandy intervals from 118 to 62 cm bsf (Figure 3). Unit II has a mottled appearance indicative of bioturbation and lacks primary sedimentary structures (Figures 3, 4A,B). Sediments within this unit are poorly to very poorly sorted, with a significant relationship between sorting and mean grain size. The cumulative frequency curves display a dominant bottom-up trend in suspended load deposition, but also feature interbedded fluctuations characterized by reduced suspended load and increased saltation load (Figure 5). These fluctuations coincide with peaks in elemental ratios such as Fe/Ca and Sr/Ca, but are anticorrelated with terrigenous elements (Si, K, and Ti) and elemental counts in Ca (Figures 3, 5A). Sediment composition in Unit II is similar to the underlying units, consisting largely of terrigenous components such as quartz and K-feldspar grains, plagioclase, and muscovite, as well as bioclasts including foraminiferal, bivalve, and gastropod shells (Figures 3, 4A,B). The abundance of bioclastic components, including shell fragments, is considerably higher within the interbedded sandy layers (Figures 3, 4A,B), where the cumulative frequency curves show an increased proportion of saltation loads (Figures 5A,B). Terrigenous elements (Si, K, Al, Ti, and Fe) exhibit a weak upward increasing trend, displaying higher values with larger fluctuations than the underlying Unit III up to 70 cm bsf (Figure 3). The values of terrigenous elements decrease upward to 50 cm bsf and then slightly increase towards the upper part of the unit (Figure 3). Similarly, Fe/Ca, Ti/Ca, and Sr/Ca ratios show an overall upward increasing trend up to 65 cm bsf, followed by an upward decreasing trend (Figure 3). Conversely, Br, Br/Ti and Mo (inc/coh) ratios exhibit anticorrelated trends with Fe/Ca and Ti/Ca ratios up to 65 cm bsf, where their trends align (Figure 3). In addition, elemental counts of Ca display an anticorrelated trend with Fe/Ca, Ti/Ca, and Sr/Ca (Figure 3).

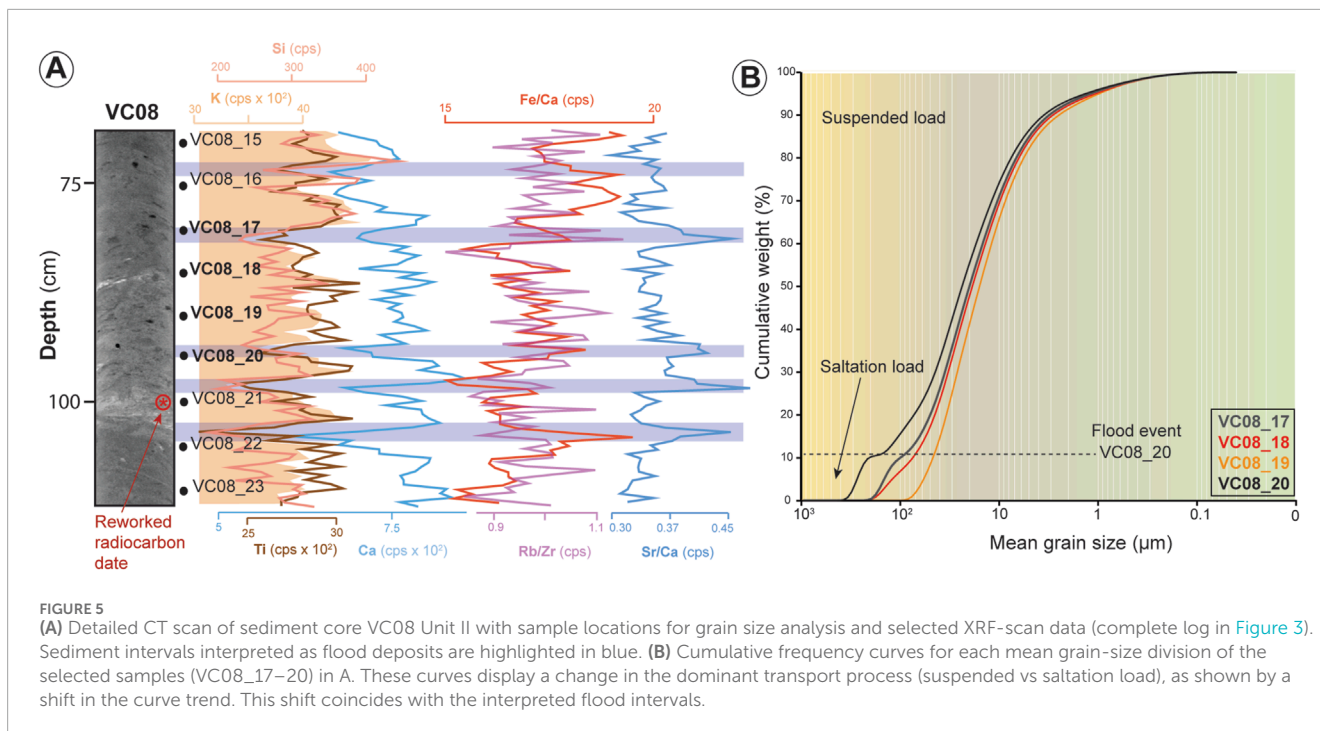
The uppermost Unit I (33–0 cm bsf) spans from around 1836 CE to the time of sediment coring (Figure 2A; Cerrillo-Escoriza et al., 2024a). Unit I is composed of mud and silty mud and exhibits an upward coarsening trend (Figure 3). In addition, an increase of the sand fraction is observed in the uppermost part of the unit (20–4 cm bsf; Figure 3). Sediments are poorly to very poorly sorted and consist largely of terrigenous and bioclastic components. Terrigenous elements (Si, K, Al, Ti, and Fe) and Ca display a weak fluctuating decreasing trend up to 4 cm bsf, followed by a subtle increasing trend towards the unit top (Figure 3). A noticeable fluctuation in this decreasing trend is observed at the bottom of the unit at 30 cm bsf, coinciding with a low peak in terrigenous elements and Ca (Figure 3). Conversely, Fe/Ca and Ti/Ca ratios display no significant variability, although a high peak coinciding with the low peak in terrigenous elements and Ca is observed (Figure 3). In contrast, Br and Br/Ti ratio, and likely Mo (inc/coh) ratio, exhibit an overall upward increasing trend (Figure 3). Additionally, Sr/Ca ratio shows no significant variability except for a high peak observed at 30 cm bsf, which also corresponds to peaks in Fe/Ca, Ti/Ca, and Br/Ti ratios (Figure 3).

4.2.2 Carchuna Canyon

Sedimentological and geochemical analyses of GC26 revealed two distinct units (Unit II and Unit I, from bottom to top; Figure 6), corresponding to the last two climatic periods over the last ~600 years. The first is the LIA from 650 to 150 cal. yr BP, and the second is the Industrial Period (IP; 150 cal yr BP–time of coring) (Figures 2B, 6).

Unit II (207–38 cm bsf) spans the entire LIA, covering at least from 454 to <100 cal. yr BP (i.e., from 1494 to <1850 CE; Figures 2B, 6). Unit II is composed of brownish green sandy/silty mud with interbedded sandy-rich intervals up to 25 cm thick (Figures 4C,D, 6). A weak fining upward trend is observed from 138 cm bsf towards the top of the unit, in agreement with clay (%) trends and Rb/Zr ratio (Figure 6). The sandy-to-silty mud sediments of Unit II are poorly to very poorly sorted, consisting predominantly of terrigenous components (Figure 6), including sub-angular grains of quartz, K-feldspar, plagioclase, and muscovite, along with bioclasts such as foraminiferal, bivalve, and gastropod shells (Figures 4C,D). These sediments exhibit a mottled appearance and the presence of burrows, indicating bioturbation, and lack primary sedimentary structures (Figures 4C,D). The interbedded sandy-rich intervals display sharp boundaries with the massive muddy sediments, with grain size gradually decreasing towards the top, forming fining-upward sequences (Figure 6). These sandy intervals exhibit sedimentary structures such as convoluted and wavy laminae. Convoluted laminae, primarily composed of fine-grained sands, often appear deforming the surrounding bioturbated, muddy sediments, exhibiting a distorted internal structure (Figures 4C,D). These intervals generally lack well-organized internal features, ripple marks are seldom observed, and wavy laminations are poorly developed or distorted (Figures 4C,D). The sandy-rich intervals also contain carbonate rock fragments and plant debris, along with minor proportions of bioclasts (Figure 4D). Terrigenous elements (Si, K, Al, Ti, and Fe) exhibit high values, interrupted by short-term fluctuations featuring lower values (Figure 6). Fe/Ca, Ti/Ca, and Sr/Ca ratios remain moderately constant up to 145 cm bsf, where they increase upward with short-term fluctuations (Figure 6). Conversely, elemental counts of Br, Br/Ti, and Mo (inc/coh) ratios exhibit anticorrelated trends with Fe/Ca and Ti/Ca ratios (Figure 6). Moreover, the elemental counts of Ca decrease from the unit bottom to 136 cm bsf, followed by moderate, nearly constant values towards the unit top (Figure 6). At the base of the sandy-rich intervals, there are notable decreases of clay (%), terrigenous elements (Si, K, Al, Ti, and Fe), Rb/Zr, Fe/Ca, Ti/Ca and Sr/Ca ratios (Figure 6). Similarly, Br, Br/Ti and Mo (inc/coh) ratios show small decreases (Figure 6). In contrast, these basal intervals are characterized by high peaks in Ca counts (Figure 6) and higher proportions of calcite (Figure 4D).

The uppermost Unit I (38–0 cm bsf) spans the most recent period, from <1980 CE to the time of sediment coring (Figure 2B; Cerrillo-Escoriza et al., 2024a). This unit, also composed of bioturbated, brownish green silty muds, shows a slight fining-upward trend above a sandy-rich basal interval (Figure 6). The sandy-rich interval is similar to those in the underlying Unit II (Figure 6) and exhibits sedimentary structures such as convoluted laminae (Figures 4C,D). These convoluted laminae, primarily composed of fine-grained sands, appears deforming the surrounding bioturbated muds, resulting in a chaotic internal



structure (Figures 4C,D). Sediments are poorly to very poorly sorted and consist largely of terrigenous and bioclastic components. Terrigenous elements (Si, K, Al, Ti, and Fe) and Ca exhibit higher values than in Unit II and a nearly constant upward trend (Figure 6). Similarly, Rb/Zr, Fe/Ca, Ti/Ca, and Sr/Ca ratios have constant values (Figure 6). In contrast, Br and Br/Ti and Mo (inc/coh) ratios exhibit an overall upward increasing trend towards the top, despite minor fluctuations (Figure 6).

4.2.3 Calahonda Canyon

Sedimentological and geochemical analyses of GC35 revealed five distinct units (Units V to I, from bottom to top; Figure 7). Despite some age uncertainties due to radiocarbon dating limitations, these units encompass the last four historical climate periods and/or transitions up to Recent times: RHIP, DA, MCA, and LIA (Figures 2C, 7). Unit V, however, extends beyond the RHIP and covers a broader time frame from ~4161 years BP. The RHIP is included in the upper part of Unit V (Figure 7).

The lowermost Unit V (235–144 cm bsf), with uncertainties due to limited ^{14}C dates, spans from ca. 6,110 to <1,138 cal yr BP (i.e., from 4,161 BCE to <812 CE; Figures 2C, 7). This unit is composed of brownish-to-brownish light green silty mud and contains three coarsening-upward intervals, with very rare primary sedimentary structures (Figure 7). Sediments along Unit V are poorly to very poorly sorted, and consist of terrigenous components, including grains of quartz, K-feldspar, plagioclase and muscovite. In addition, bioclasts such as foraminiferal, bivalve and gastropod shells, as well as mottling indicative of bioturbation (Figures 7, 4E,F), are observed throughout the unit. Terrigenous elements (Si, K, Al, Ti and Fe), clay (%), Ca, and Rb/Zr, Fe/Ca, Ti/Ca, and Sr/Ca ratios exhibit high values with minor short-term fluctuations (Figure 7). Major fluctuations roughly coincide with the coarsening-upward intervals.

Similarly, Br and Br/Ti and Mo (inc/coh) ratios remain stable but slightly fluctuating (Figure 7).

Unit IV (144–125 cm bsf) likely covers the DA (Figures 2C, 7). This unit is composed of brownish light green mud/silty mud with homogeneous composition of the coarse and fine fractions. This unit is poorly sorted, largely composed of terrigenous components along with foraminiferal and mollusk shells, and it exhibits a mottled appearance lacking primary sedimentary structures (Figure 7). Likewise, terrigenous elements (Si, K, Al, Ti, and Fe), Br and Rb/Zr, Br/Ti, and Sr/Ca Mo (inc/coh) ratios display a relatively stable and homogeneous trend (Figure 7). Conversely, Fe/Ca and Ti/Ca ratios show an upward increasing trend. Elemental counts of Ca display an anticorrelated trend with Fe/Ca and Ti/Ca ratios (Figure 7).

Unit III (125–95 cm bsf) likely covers the MCA (Figures 2C, 7). This unit is composed of brownish light green mud. Similar to underlying Unit IV, this unit is poorly sorted, largely composed of terrigenous components along with shell bioclasts, and it exhibits a mottled appearance with no primary sedimentary structures (Figure 7). Unit III exhibits constant geochemical values (Figure 7).

Unit II (95–25 cm bsf) spans the LIA (Figures 2C, 7). This unit consists of bioturbated brownish green mud/silty mud, exhibiting a weak fining-upward trend from a sandy-rich basal interval up to 65 cm bsf. Above 65 cm bsf, a weak coarsening-upward trend is observed, accompanied by interbedded coarse-grained intervals from 44 cm bsf to the top (Figure 7). Sediments of Unit II are poorly sorted, primarily composed of terrigenous components, along with shell bioclasts. Abundance of bioclastic components is higher within the coarse-grained intervals. The unit exhibits a mottled appearance indicative of bioturbation and lacks primary sedimentary structures (Figures 4E,F, 7). Terrigenous elements (Si, K, Al, Ti, and Fe), Ca and Rb/Zr display high values with minor, short-term fluctuations up to 44 cm bsf, above which they slightly decrease towards the unit top,

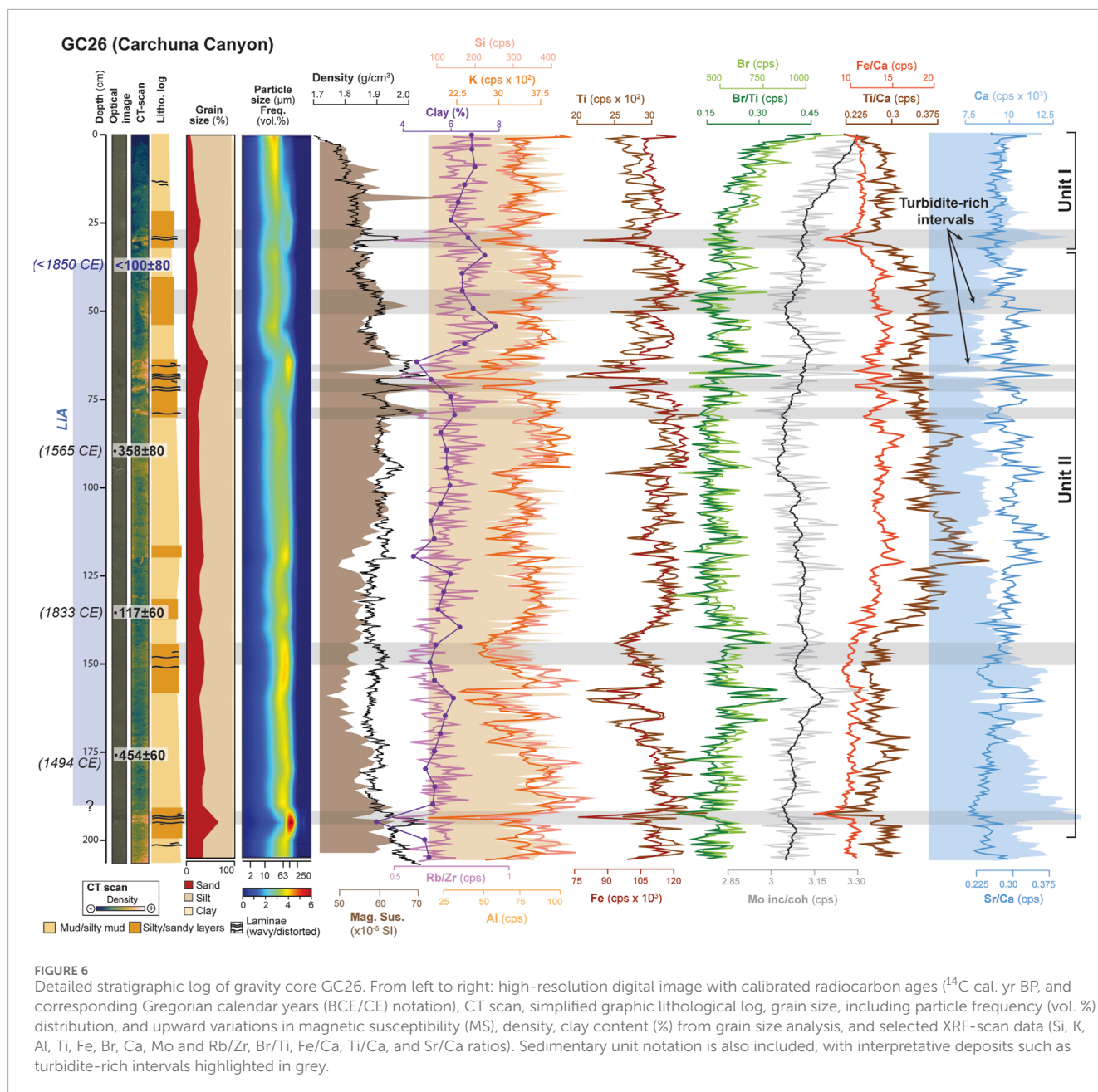


FIGURE 6
Detailed stratigraphic log of gravity core GC26. From left to right: high-resolution digital image with calibrated radiocarbon ages (¹⁴C cal. yr BP, and corresponding Gregorian calendar years (BCE/CE) notation), CT scan, simplified graphic lithological log, grain size, including particle frequency (vol. %) distribution, and upward variations in magnetic susceptibility (MS), density, clay content (%) from grain size analysis, and selected XRF-scan data (Si, K, Al, Ti, Fe, Br, Ca, Mo and Rb/Zr, Br/Ti, Fe/Ca, Ti/Ca, and Sr/Ca ratios). Sedimentary unit notation is also included, with interpretative deposits such as turbidite-rich intervals highlighted in grey.

with a pronounced decrease in Rb/Zr ratio (Figure 7). Conversely, Fe/Ca, Ti/Ca, and Sr/Ca ratios display an upward increasing trend, as Br, Br/Ti, and Mo (inc/coh) ratios (Figure 7). Furthermore, significant fluctuations occur within the coarse-grained intervals from 44 cm bsf to the top of the unit (Figure 7).

Unit I (25–0 cm bsf) spans the most recent period, from <1880 CE to the time of sediment coring (Figure 2C; Cerrillo-Escoriza et al., 2024a). The sediments at the core top consist of mud/silty mud exhibiting a weak fining-upward trend. This unit is also poorly sorted, largely composed of terrigenous components along with shell bioclasts, and exhibits a mottled appearance with rare occurrences of primary sedimentary structures (Figures 4E,F, 7). Geochemical proxies display a relatively constant, yet fluctuating trend (Figure 7).

5 Interpretation and discussion

5.1 Depositional environments: differences between canyons

Marked differences between the Motril, Carchuna, and Calahonda canyon depositional environments are found (Figures 1B,C), likely triggered by distinct fluvial, hydrodynamic and sediment transport influences, as discussed below.

5.1.1 The Motril Canyon: a recent sediment trap

In the Motril Canyon, sedimentation over the last ~2000 years BP was dominated by muddy, fine-grained sediments with high

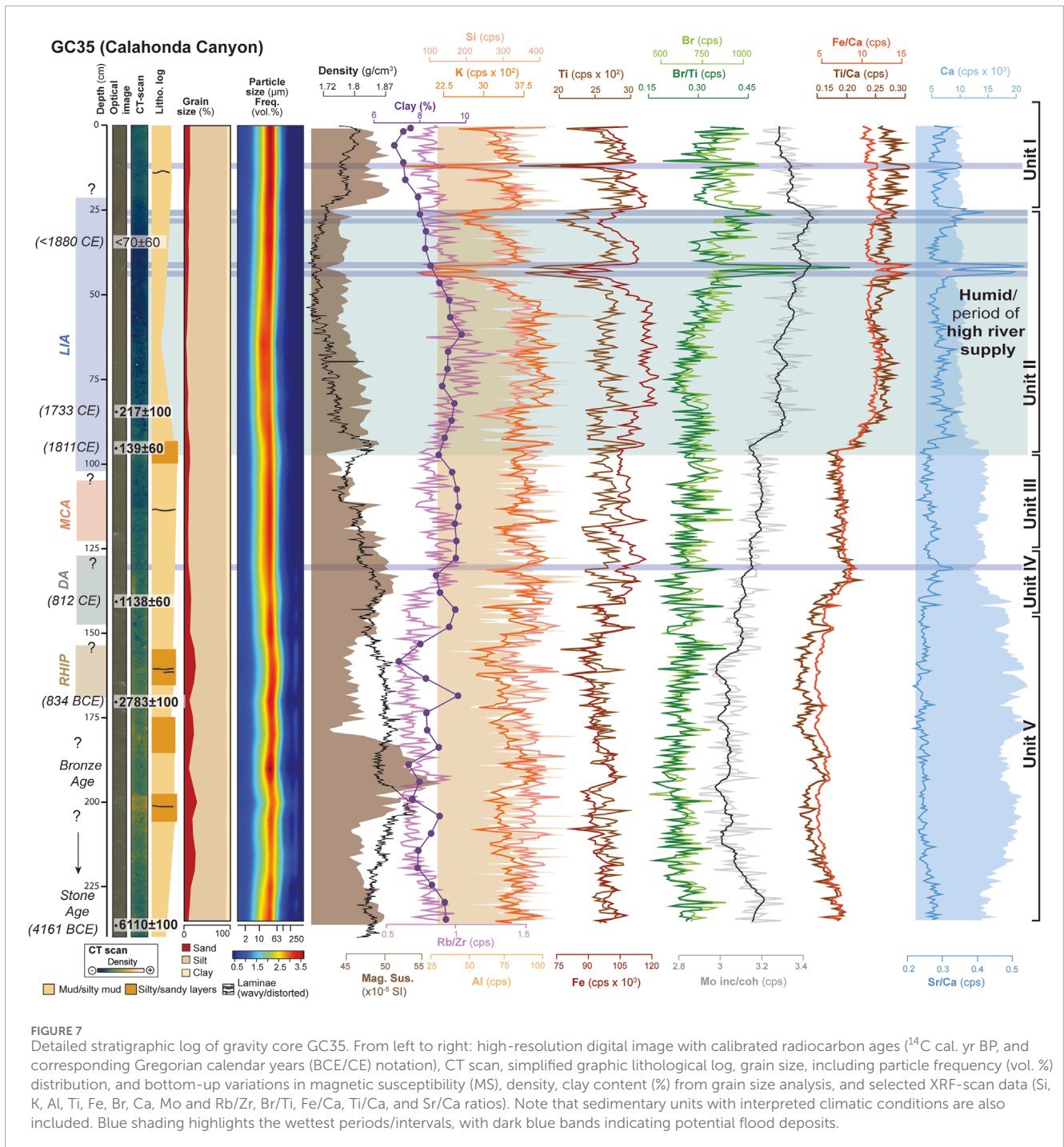


FIGURE 7
 Detailed stratigraphic log of gravity core GC35. From left to right: high-resolution digital image with calibrated radiocarbon ages (¹⁴C cal. yr BP, and corresponding Gregorian calendar years (BCE/CE) notation), CT scan, simplified graphic lithological log, grain size, including particle frequency (vol. %) distribution, and bottom-up variations in magnetic susceptibility (MS), density, clay content (%) from grain size analysis, and selected XRF-scan data (Si, K, Al, Ti, Fe, Br, Ca, Mo and Rb/Zr, Br/Ti, Fe/Ca, Ti/Ca, and Sr/Ca ratios). Note that sedimentary units with interpreted climatic conditions are also included. Blue shading highlights the wettest periods/intervals, with dark blue bands indicating potential flood deposits.

accumulation rates (Figures 2A, 3). Notably, high values of Ca, coupled with moderate to high values of terrigenous elements, mostly in units V, III and I (Figure 3), suggest that detrital carbonate from limestone/dolostone outcrops, most likely from the Alpujarride Complex (Figure 1C; Aldaya et al., 1979; 1981), may have served as a Ca-bearing sediment source transported through the Guadalfeo River drainage system. High sedimentation and mass accumulation rates (1.45 cm·yr⁻¹ and 15.21 kg·m⁻² yr⁻¹) have also been reported in the recent sedimentary record of the Motril canyon (see Figure 9B in Cerrillo-Escoriza et al., 2024a).

These high accumulation rates, along with the predominance of fine-grained sediments—primarily deposited by suspended load and relatively enriched in mica, terrigenous elements, and organic matter (Figures 3–5)—are typically associated with episodic flooding events (e.g., Mendes et al., 2020). The increasing Fe/Ca and Ti/Ca ratios suggest that the main flooding events occurred during Unit II deposition (Figure 3), which may have been driven by river-derived sediment density flows comparable to hyperpycnites (e.g., Mulder et al., 2003). Similar sedimentary patterns have been observed in other inner-shelf systems along the southern

Iberian Peninsula (e.g., Mendes et al., 2020) and elsewhere (e.g., de Mahiques et al., 2009; Mojtahid et al., 2018). Fine-grained transport during flood events is interpreted to have occurred primarily via suspension load, though there is also evidence for some degree of saltation (e.g., see detailed frequency curves of Unit II in Figure 5). This is reflected in increases in the sand-sized fraction and Sr/Ca ratios, and a decrease in Ca, indicating reduced inputs of detrital carbonate (e.g., Hodell et al., 2008; Rothwell and Croudace, 2015) (Figures 3, 5A). The coarse grains interpreted as the product of saltation load are mainly composed by bioclasts, such as bivalve shells and benthic foraminifera (Figure 4B). This suggests that the observed increases in grain size could have been driven by higher concentrations of bioclasts. Indeed, Ca and Sr are associated with biogenic inputs, especially from bivalve and gastropod shells, with Sr being linked to aragonitic shells (e.g., Hillaire-Marcel and De Vernal, 2007). Shell fragmentation also suggests some degree of downslope sediment transport (Figure 4B). The bioclast increase, particularly of coarse-sized shells and shell fragments, most likely reflects increased benthic production occurring in shallower areas. There, increased river discharges could have enhanced sediment erosion and redistribution. These bioclasts would have been transported to greater depths, where they eventually accumulated. This interpretation is consistent with the notion that fluvial input can enhance benthic productivity in proximal areas, while hydrodynamic processes facilitate the downslope transport and deposition of coarse biogenic material (e.g., Mendes et al., 2020).

The absence of primary sedimentary structures or evidences of sediment reworking (Figures 3, 4A,B) suggest that deposition primarily occurred under low-energy hydrodynamic conditions. Moreover, sediment remobilization seems to be of minor importance, as the radiocarbon dates, except for one outlier at 100 cm bsf, consistently increase with core depth (Table 1; Figures 2A, 3). This aligns with observations of terrigenous-dominated regions influenced by riverine input during periods of reduced marine winnowing (e.g., Sommerfield et al., 2002; Sommerfield and Wheatcroft, 2007). Further evidence supporting limited sediment transport through the Motril Canyon is given by the absence of transported shelf benthic foraminifera in recent canyon sediments (Cerrillo-Escoriza et al., 2024a). We thus interpret the Motril Canyon primarily functioned as a river-fed system, strongly influenced by fluvial discharges of the Guadalfeo River (Figures 1B,C) during periods of calm hydrodynamic conditions in the last 350 cal. yr BP (Figure 3). The Motril Canyon thus acted as a sediment trap, and therefore its recent sedimentary infill enables the reconstruction of natural and human-induced Holocene paleoenvironmental changes (see Section 5.2. below).

5.1.2 The Carchuna Canyon: sediment pirating from the littoral cell

Sediment deposition in the Carchuna Canyon is mainly characterized by coarse-grained facies and very thin to thin-bedded, fine-grained, mica-rich sandy turbidites (Figures 4C,D, 6), which are often enriched in carbonaceous fragments (Figures 4C,D). These fine-grained turbidites, often exhibiting convoluted laminae (Figures 4D–7), are predominantly found within Unit II, with some also present at the base of Unit I (Figure 6). They are interpreted as deposited from turbulent flows in which particles were primarily transported by saltation and rapidly settled (e.g., Lowe, 1979; Stow

and Smillie, 2020). Moreover, the high Ca contents, coupled with the occurrence of carbonaceous fragments (Figures 4D, 6), suggests that limestone and dolostone outcrops adjacent to the Carchuna Canyon head provided significant coarse-grained sediment inputs to the regional littoral cell (Figure 1C). Given the location of these outcrops, it is more likely that their redistribution was primarily driven by westward littoral currents under the dominance of easterly winds. Additionally, the Alpujarride Complex may have served as a Ca-bearing source of sediments transported through the Guadalfeo drainage basin (Figure 1C; Aldaya et al., 1979; 1981).

Consequently, the observed sedimentary features suggest transport activity driven by turbidity flows along the Carchuna Canyon during the last 500 years. This interpretation agrees with previously evidence (Cerrillo-Escoriza et al., 2023; 2024a; 2024b): (a) the coarse composition of surficial sediments in the axial channel; (b) low mass accumulation rates ($5.40 \text{ kg}\cdot\text{m}^{-2} \text{ yr}^{-1}$) in the axial channel with a sedimentation rate of $0.49 \text{ cm}\cdot\text{yr}^{-1}$; (c) high organic matter contents at both the termination of the upper canyon segment (between 350 and 400 m water depth) and the lower canyon segment; (d) the occurrence of marine litter accumulations in the upper canyon segment; (e) identification of bedforms along the axial channel and the adjacent depositional lobe, which are also attributed to high-density turbidity currents; (f) high values of transported shelf benthic foraminifera in the lower canyon segment.

We interpret that longshore drift and wave focusing in the Carchuna Canyon head (Figure 1; Ortega-Sánchez et al., 2014; Cerrillo-Escoriza et al., 2024a) have mobilized coarse-grained sediments subsequently transported by turbidity currents. These transport dynamics are consistent with those observed in littoral systems where canyon heads act as focal points for sediment winnowing and bypassing (e.g., Smith et al., 2018). The limited fluvial discharge of Puntalón ravine to the west (Figure 1B), combined with the energetic wave regime—often amplified by the local irregular seafloor (Cerrillo-Escoriza et al., 2023; 2024a; 2024b)—suggests that, over the last 500 years, sediment transport and deposition in the Carchuna Canyon have been primarily controlled by westward-directed longshore drift, in contrast to the fluvially influenced Motril Canyon. However, other potential triggers for turbidity currents, such as earthquake-induced sediment remobilization, cannot be ruled out. In tectonically active margins, earthquake shaking is known to induce synchronous slope failures across broad regions, generating diagnostic turbidite layers used to reconstruct seismic recurrence intervals (e.g., Goldfinger et al., 2003; Goldfinger et al., 2012; 2013; Moernaut et al., 2014). These earthquake-triggered flows or “seismoturbidites” are commonly funneled through submarine canyons and deposited on the basin floor (e.g., Goldfinger et al., 2012; 2013). The southern Iberian Peninsula, and particularly the SW margin, has experienced significant historical earthquakes over the last 500 years, most notably the well documented 1755 CE Lisbon earthquake and tsunami event (see review by Lario et al., 2011; Álvarez-Martí-Aguilar, 2022). Locally, historical earthquakes have also occurred in nearby coastal towns, such as the 1679 CE Andalusian earthquake and the 1804 CE Motril earthquake (Museo de Historia de Motril, 2023). Therefore, it is plausible that some of the fine-grained turbidites observed at GC26 Unit II (Figure 6) may correspond to such local seismic events, although further chronological and stratigraphic correlation is required to confirm this interpretation.

In comparable environments, shelf failures have typically been associated with sediment overloading during storms (e.g., Puig et al., 2004), or with ground shaking and instability caused by regional earthquakes (e.g., Mulder et al., 1998; Goldfinger et al., 2012; 2013).

5.1.3 The Calahonda Canyon: a mixed system

Finally, recent sedimentation in the Calahonda Canyon reflects an intermediate depositional environment between the Motril and Carchuna canyons. Its sedimentary archive includes a mixture of muddy, fine-grained facies, and coarse-grained deposits (Figures 4, 7), indicating a depositional environment likely influenced by both fluvial inputs and bi-directional hydrodynamic processes. The shelf east of the Calahonda Canyon is primarily influenced by easterly winds (e.g., Ortega-Sánchez et al., 2014; Cerrillo-Escoriza et al., 2024a), able to generate westward-directed shelf currents which most likely transported and deposited coarse-grained sediments, including turbidites. Yet moderate eastward currents formed during westerlies dominance, reaching velocities up to $0.5 \text{ m}\cdot\text{s}^{-1}$ [see Figure 12A in Cerrillo-Escoriza et al. (2024a)], may also have supplied moderate amounts of sediment. In addition, the adjacent shelf is supplied by small water courses, such as the Gualchos ravine located 5 km to the east (Figure 1B), and the more distant Adra River about 40 km further east. While the Gualchos ravine may provide seasonal, discontinuous sediment input, the Adra River is likely to deliver moderate to limited sediment discharges, with much of its sediment load confined to its proximal deltaic environment (Mendes et al., 2015; Bárcenas et al., 2024). Sediment may be laterally transported by west-southwest-directed longshore drift, driven by the prevailing easterly winds and the rectilinear coastal morphology (Lario et al., 1999), and are eventually trapped at the Calahonda Canyon (Figures 1B, 7). This suggests that the Calahonda Canyon has likely functioned as a longshore-drifted system, receiving sediment input from both littoral currents that mobilize coarse-grained sediments—ultimately transported by turbidity currents—and from ephemeral, seasonal streams with intermittent flows. Additionally, the Adra River may have provided moderate amounts of sediment under the influence of easterly winds. Thus, despite the presence of interbedded gravity-driven deposits, the sedimentary infill of the Calahonda Canyon holds potential for reconstructing natural and human-induced Holocene paleoenvironmental changes.

5.2 The late Holocene depositional record in a sediment trap off the Guadalfeo submarine delta

The long-term depositional evolution off the Guadalfeo submarine delta (Figure 1B), spanning from ca. 6110 cal. yr BP (4161 BCE) to the present, has been recorded in our sedimentary archives (Figures 3–7). However, the period between ~6000 and 2000 years BP was only recorded in the Calahonda Canyon, which requires more precise age constraints (Figures 2, 7). As a result, we have focused on the depositional record of the last ~2000 years BP. This reconstruction is primarily based on the sedimentary archive of the Motril Canyon (Figure 1B), which has functioned as an effective sediment trap and provides the most continuous sediment record for the last ~2000 years (Figure 3).

Our results have revealed four main evolutionary stages, which largely correspond to the last four historical climate periods described below. These stages reflect major changes in sediment production within the hinterland. Given the lack of consensus in the literature about the chronology for these four climatic stages (e.g., see Helama et al., 2017), here we follow the chronology proposed by Moreno et al. (2012).

5.2.1 The Iberian-Roman humid period (IRHP)

The IRHP (2600–1600 cal. yr BP), described as a wet period (Martín-Puertas et al., 2009), is widely recognized in the southern Iberian Peninsula (e.g., García-Alix et al., 2013; Jiménez-Moreno et al., 2013; Ramos-Román et al., 2018; López-Avilés et al., 2021). There, pollen records from the Sierra Nevada wetland (e.g., Laguna Hondera; Ramos-Román et al., 2018) have extended the IRHP to 2600–1450 cal. yr BP. Within this broad humid phase, an arid Roman Empire Epoch—known as the “Roman Climatic Optimum” (2150–1800 cal. yr BP; McCormick et al., 2012; Bini et al., 2020)—has been reported, likely influenced by both climatic forcing and human activity. This arid interval is also recorded in the Sierra Nevada wetland (e.g., between 2300 and 1800 cal yr BP; Ramos-Román et al., 2018; or between 2400 and 1900 cal yr BP; Ramos-Román et al., 2016).

The IRHP was recorded in the Motril and Calahonda canyons (Figure 1B), albeit with limited radiocarbon ages (Figures 2, 3, 7). In the Motril Canyon, the recorded IRHP spanning from ~2025 to 1500 cal. yr BP would coincide with the arid Roman Empire Epoch (McCormick et al., 2012; Bini et al., 2020). During this period, sedimentation was dominated by coarse-grained fractions and relatively low sedimentation rates (Figure 3), suggesting a reduced terrigenous suspension input (Durand et al., 2018; Mendes et al., 2020). This interpretation is supported by moderate elemental counts of Si, K, Ti, and Al, as well as by Fe/Ca and Ti/Ca ratios (Figures 3, 7), indicating reduced terrigenous sediment input due to limited Guadalfeo River discharges (Figure 1B). This inference agrees with suggested slow advances of the Guadalfeo deltaic system with rates of $\sim 0.15 \text{ m}\cdot\text{yr}^{-1}$ during the IRHP and later (between 2000 BCE and 1500 CE; Jabaloy-Sánchez et al., 2014). The establishment of dry conditions could explain this limited continental export, as interpreted in other shelf environments (e.g., de Mahiques et al., 2009).

The Motril Canyon recorded a shift towards finer-grained sedimentation and an increase in fluvial elemental ratios at the end of the IRHP (Figure 3), suggesting a transition to more humid conditions. This pattern is broadly synchronous with a humid phase that occurred during the decline of the Roman Empire between 1800 and 1600 cal. yr BP, likely associated with negative North Atlantic Oscillation (NAO) conditions that increased the influence of westerly winds over southern Europe, thereby enhancing moisture levels (e.g., Olsen et al., 2012).

Although the end of the IRHP was marked by increased moisture availability, the increase in terrigenous sediment export may have been influenced by additional factors, including intensified human land use. This assumption aligns with the limited flood activity recorded in the southwest Iberian Peninsula during this period (e.g., Thorndycraft and Benito, 2006; Benito et al., 2015; Mendes et al., 2020). During the Roman Empire, the effects of anthropogenic activities such as mining, agricultural and grazing

activities on sediment production have been documented in the Iberian Peninsula, even at high altitudes in the southeastern region (e.g., Leblanc et al., 2000; Boone and Worman, 2007; García-Alix et al., 2013; Jiménez-Moreno et al., 2013; Ramos-Román et al., 2016; 2018; López-Avilés et al., 2021; Díez-Herrero et al., 2024). For example, mining exploitation of copper, silver, and gold increased significantly since ~2500 cal. yr BP (Leblanc et al., 2000), with a peak in activity occurring between 0 and 200 CE (2000–1800 cal. yr BP; Davis et al., 2000; Delgado et al., 2012).

5.2.2 Dark ages (DA)

Between 1500 and 1000 cal. yr BP, the climate in northern Europe experienced a deterioration characterized by rapid cooling and aridification, a period commonly referred to as the Dark Ages (e.g., Magny, 2004; Regattieri et al., 2014). Pollen records from the central and southern Iberian Peninsula also suggest that arid conditions prevailed during the DA (e.g., Carrión, 2002; Jiménez-Moreno et al., 2013; Ramos-Román et al., 2016; Ramos-Román et al., 2018). Similar climatic conditions have been detected in marine records from the Alboran Sea (Fletcher and Sánchez-Goñi, 2008; Combourieu-Nebout et al., 2009; Nieto-Moreno et al., 2013; 2015).

Off the Guadalfeo delta system, this period was recorded and dated in the Motril Canyon (Figure 3). Initially, sedimentation during the DA was characterized by coarse-grained fractions akin to those deposited during the preceding IRHP. However, a gradual transition to fine-grained sediment deposition occurred, accompanied by increased sedimentation rates, and coherent with increases in elemental counts of Si, K, Ti, and Al, as well as Fe/Ca and Ti/Ca ratios (Figure 3). This suggests a gradual rise in terrigenous suspension input to the shallow-marine environment, likely driven by changes in sediment production in the hinterland. The rise in fine-grained sediment input could be related to moderate rainfall conditions in the Guadalfeo River basin. Comparable evidence of moderate rainfall has also been reported in other southern Iberian basins, such as the Guadiana Basin, which recorded flood activity between ~1200 and 1000 cal. yr BP (Ortega and Garzón, 2009; Benito et al., 2008; 2015; Mendes et al., 2020). However, a positive NAO phase during this period may have contributed to increase aridification over the Guadalfeo River region (Trouet et al., 2009; Olsen et al., 2012).

As a result, factors other than climatic changes may have triggered the rise in terrigenous sediment supply to the Guadalfeo delta system. Widespread soil erosion and land degradation caused by intensified land use appear to have largely contributed to the sediment increase. Historical accounts suggest that the decline of Roman influence in Iberia at ca. 1500 cal. yr BP initiated a period of significant demographic changes. In fact, settlement density in southwestern Iberian Peninsula increased sixfold during the following 500 years, particularly after the Muslim invasion at ca. 1200 cal. yr BP (Boone and Worman, 2007). Such intensified land use likely exacerbated soil erosion, contributing to the increase in terrigenous sediment supply to the Guadalfeo delta (e.g., Jabaloy-Sánchez et al., 2014). A similar phenomenon occurred in the central Adriatic, where sedimentation rates quadrupled between 1100 and 700 cal. yr BP due to changes in land use that enhanced terrigenous sediment input to the shelf (Oldfield et al., 2003).

5.2.3 Medieval climate anomaly (MCA)

The MCA (1050–650 cal. yr BP) was characterized by warm conditions driven by a persistent positive NAO (e.g., Trouet et al., 2009; Moreno et al., 2012; Olsen et al., 2012). In the southern Iberian Peninsula, several pollen records document a warmer and relatively arid climate during the MCA (e.g., Jiménez-Moreno et al., 2013; Ramos-Román et al., 2016; 2018; Ramos-Román et al., 2018). These arid conditions were associated with a low frequency of floods and reduced fluvial inputs to marine basins (Moreno et al., 2012, and references therein). Evidence of drought is particularly well documented in sediment records from Sierra Nevada wetlands, such as the Laguna de la Mula (e.g., Jiménez-Moreno et al., 2013).

Off the Guadalfeo delta system, the MCA is also recorded in the Motril Canyon (Figure 3). Sedimentation during the MCA was predominantly fine-grained, with higher sedimentation rates compared to the DA (Figure 3). Our proxy data suggest a sustained influx of terrigenous material into the shallow-marine environment, driven by persistent sediment production in the hinterland. Although sedimentation patterns were broadly similar during the DA and MCA periods, evidence of moderate rainfall conditions appears less pronounced during the MCA (Figure 3). This suggests that widespread soil erosion and land degradation—primarily due to intensified human land use—played a significant role in increasing terrigenous sediment production. Despite generally dry conditions, geoaerological studies from the southeastern Iberian Peninsula have identified notable paleo-flood events during the Andalusian Almohad Taifa period (late 12th to early 13th century CE) (Díez-Herrero et al., 2024). A stunning example is the “Roman theatre of Acci” (modern-day Guadix), which preserves evidence of extreme hydrological events associated with the Medieval Warm Period. While such findings suggest the possibility of small, localized episodes of anomalous rainfall conditions, such events would have been sporadic and restricted regionally (e.g., Ortega and Garzón, 2009; Benito et al., 2008; 2015; Mendes et al., 2020), consistent with the influence of NAO dynamics on moisture availability throughout most of Iberia (Sánchez-López et al., 2016).

In terms of anthropogenic effects on sediment production, major land-use changes—including deforestation, cultivation, and agricultural intensification—initiated approximately 200 years prior to the MCA (Boone and Worman, 2007). These practices likely contributed to increase the sediment supply to the shelf. In the southwestern Iberian Peninsula, this drastic land surface degradation led to the abandonment of most rural settlements by the mid-12th century CE (ca. 800 cal. yr BP; e.g., Boone and Worman, 2007). Consequently, the combined impact of arid conditions and human-driven landscape changes accelerated soil erosion during the MCA, increasing terrigenous sediment export to the Guadalfeo delta system.

5.2.4 Little ice age (LIA) to recent times

Two climatically distinct periods can be distinguished over the last ~600 years. The first is the LIA from 650 to 150 cal. yr BP, and the second is the Industrial Period (IP; 150 cal yr BP–present). The LIA is interpreted as an overall humid period in the Guadalfeo region (Figure 1B). In the studied sediment cores, this period is recorded in the Motril, Carchuna, and Calahonda canyons (Figures 3, 6, 7). This period is marked by high rates of fine-grained sediment deposition, suggesting increased terrigenous input of suspension loads. This

interpretation is supported by the occurrence of increased elemental counts of Si, K, Ti, and Al, as well as by high Fe/Ca and Ti/Ca ratios (Figures 3, 6, 7). The increase in fine-grained sediment supply to the continental shelf during the LIA likely reflects a period of increased rainfall in the Guadalfeo River basin, correlated with a negative NAO phase (e.g., Trouet et al., 2009; Fletcher et al., 2013). This trend is consistent with the suggested rapid advancement of the Guadalfeo Delta, at rates of $\sim 3.3 \text{ m yr}^{-1}$ from 1500 CE to the present day (Jabaloy-Sánchez et al., 2014).

An increase of fluvially derived proxies has been previously documented in the Alboran Sea (e.g., Nieto-Moreno et al., 2011; 2015) and in inland records (e.g., Moreno et al., 2012; Ramos-Román et al., 2016; Ramos-Román et al., 2018). Equivalent phases of fine-grained deposition driven by enhanced river discharges have been documented elsewhere during the LIA (Abrantes et al., 2005; Lebreiro et al., 2006; Bartels-Jónsdóttir et al., 2006; 2015; Mendes et al., 2020). Pollen fluctuations in several Iberian records suggest that the LIA was not a climatically stable period, and numerous short-term oscillations occurred (e.g., Ramos-Román et al., 2016; García-Alix et al., 2017; Oliva et al., 2018). It is also worth mentioning that the humid conditions inferred from our LIA records coincide with rainfall reconstructions for the past 500 years in southern Iberia based on documentary sources (e.g., Rodrigo et al., 1999; Sánchez-García et al., 2019; Sánchez-García and Schulte, 2023). Historical flood records from the southern Iberian Peninsula have revealed alternating periods of increased (e.g., 1540–1560, 1720–1745, and 1860–1891) and decreased (1790–1845) flood frequencies. Additionally, human activities during the LIA also impacted the southern Iberian Peninsula. For instance, the expansion of cereal agriculture and transhumant livestock practices between the 16th and 19th centuries CE led to episodes of extensive soil erosion (e.g., García-Ruiz, 2010). Furthermore, demographic changes and mining activities during the 18th and 19th centuries CE resulted in a significant deforestation of the Iberian Peninsula (Martín-Rosales et al., 2007).

Humid conditions prevailed during most of the IP and into the early 20th century CE in the southern Iberian Peninsula, as evidenced by instrumental precipitation data (Rodrigo et al., 1999; Sánchez-García et al., 2019; Sánchez-García and Schulte, 2023). However, increased local aridity and/or human-induced desertification is reported in the Sierra Nevada wetland records (e.g., García-Alix et al., 2013; Ramos-Román et al., 2016). Indeed, a general decreasing trend of rainfall has been observed in the southern Iberian region from 1960 onwards (Rodrigo et al., 1999), as well as elsewhere in the Iberian Peninsula (Gallego et al., 2011; Rodrigo and Trigo, 2007) during the last century. Our sedimentary record at Motril Canyon shows a general decrease in fluvial-derived material during the IP (Figure 3), suggesting a diminished supply from the Guadalfeo River.

5.3 Comparison with terrestrial and deep-marine record: a source-to-sink approach

To evaluate the coupling between shelf sediment storage and downslope transfer under the influence of Late Holocene climatic fluctuations, we compared our results from the Motril

and Calahonda canyons with existing terrestrial and deep-water sediment records (Figure 8).

K/Ti ratios from the Sierra Nevada wetland sedimentary records reveal lithological changes linked to variations in local depositional environments and allochthonous sediment inputs (García-Alix et al., 2018). As the regional drainage basin is dominated by metamorphic mica schists, rich in Si, K, and Al (Camuera et al., 2018), the K/Ti ratio serves as a robust proxy for detrital inputs and surface runoff (e.g., Ramos-Román et al., 2018). Similarly, Ti/Ca and Fe/Ca ratios have also been reported as tracers of terrigenous supply and/or riverine input in marine environments (e.g., Mendes et al., 2020; Mesa-Fernández et al., 2022). In the Sierra Nevada wetland, higher K/Ti ratios indicate wetter conditions dominated by runoff, while lower values correspond to increased aridity and a predominance of aeolian inputs (Figure 8; Ramos-Román et al., 2018). These fluctuations are reflected in arboreal pollen datasets, which record shifts in forest cover and humidity. Periods of increased arboreal pollen abundance correlate with humid conditions and forest expansion, as observed during the end of the DA and the LIA, whereas declines in arboreal pollen, such as around 1200 cal. yr BP and during the MCA, align with severe droughts (Figure 8; Jiménez-Moreno et al., 2013; Ramos-Román et al., 2016; 2018; Ramos-Román et al., 2018).

In the shallow-marine environment, the sediment records from the Motril and Calahonda canyons exhibit variability in Ti/Ca and Fe/Ca ratios, which serve as tracers of terrigenous input related to riverine discharges to the shelf. During wetter periods, such as the LIA (~ 600 –150 cal. yr BP), Ti/Ca and Fe/Ca ratios increased notably, reflecting enhanced sediment delivery due to intensified river runoff (Figure 8). An increase in Ti/Ca and Fe/Ca ratios also occurred from the late DA to the DA-MCA transition (at ~ 1016 cal. yr BP; Figure 8), suggesting moderate hinterland precipitation/river runoff. These humid phases are likely linked to persistent negative NAO conditions, which promoted increased precipitation in the western Mediterranean Basin (Trouet et al., 2009; Fletcher et al., 2013). Conversely, drier conditions during the MCA, driven by a persistent positive NAO phase (Trouet et al., 2009; Olsen et al., 2012; Moreno et al., 2012), resulted in lower Ti/Ca and Fe/Ca ratios (Figure 8), indicating reduced riverine sediment fluxes.

In the deep marine environment, sedimentary archives from the western Alboran basin display a sharp increase in Ti/Ca ratios during the onset of the DA at around 1500 years BP (Figure 8; Mesa-Fernández et al., 2022), during a period of increasing aridity (e.g., Trouet et al., 2009; Olsen et al., 2012), suggesting that the enhanced sediment delivery to the western Alboran Basin was not primarily driven by riverine discharges. Instead, the timing of this increase aligns with the dissolution of Roman control in Iberia, which likely intensified human-induced landscape modification. Therefore, increased land use and deforestation, leading to widespread erosion, appear to have caused the greater terrigenous sediment input to marine basins. Increased Western Mediterranean Deep-Water formation at that time likely enhanced sediment transport to the deep basin (Mesa-Fernández et al., 2022). Sedimentary records from the western Alboran Basin also indicate a sustained transfer of terrigenous sediments to the deep sea throughout the MCA and the LIA that persist to the present (Figure 8). A comparable increase in terrigenous input is also recorded after 2000 years BP in other Late Holocene marine records

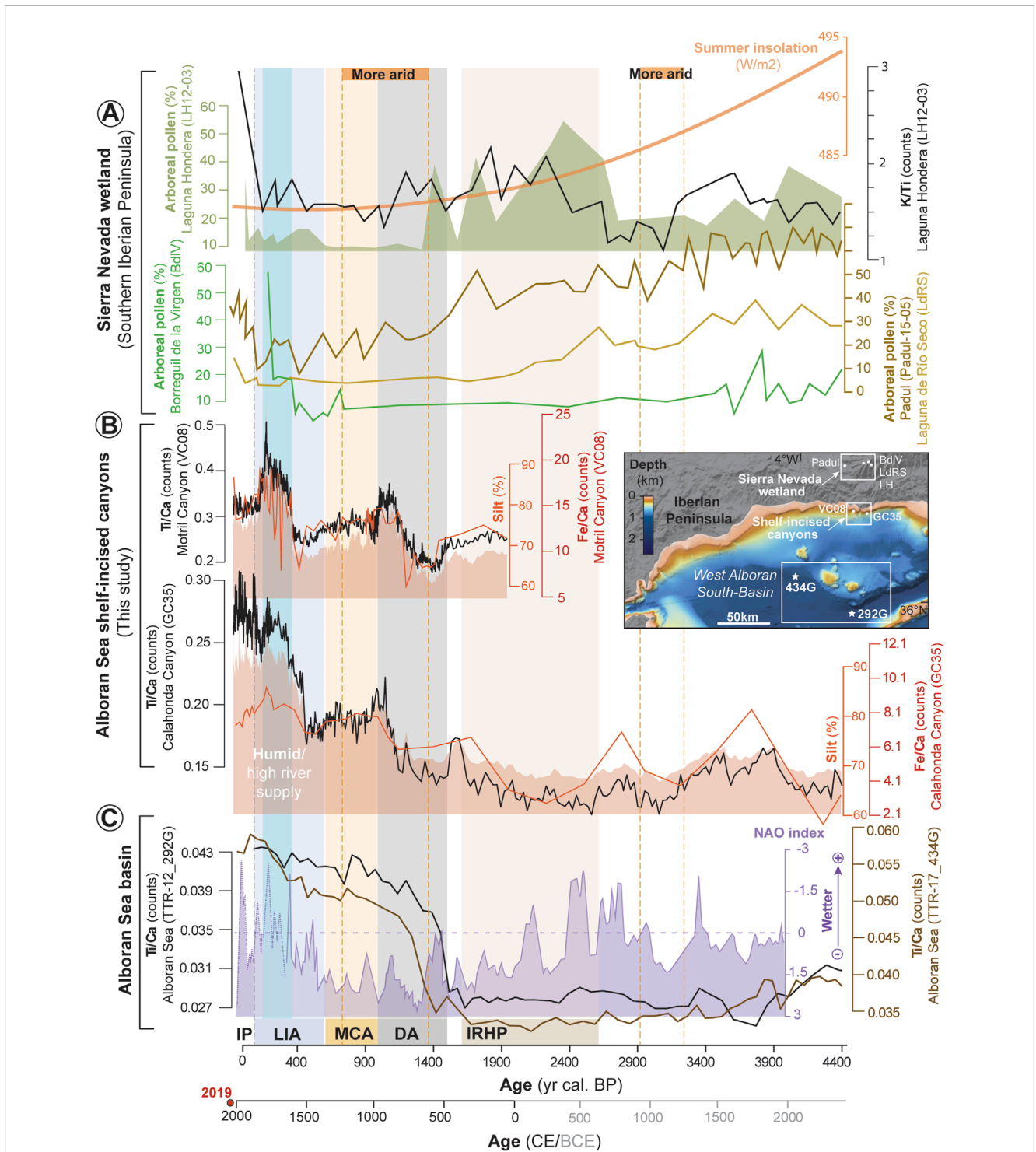


FIGURE 8 Comparison of sedimentary records from terrestrial (Sierra Nevada wetland), shallow-marine (shelf-incised canyons of the Alboran Sea—this study), and deep-marine (Alboran Sea basin) environments. **(A)** Terrestrial records from the Sierra Nevada wetland displaying arboreal pollen variations. These records include the sediment cores: LH12-03 from Laguna Hondera (Mesa-Fernández et al., 2018), BdlV from Borreguil de la Virgen (Jiménez-Moreno and Anderson, 2012), Padul-15-05 from Padul (Ramos-Román et al., 2018), and LdRS from Laguna de Rio Seco (Anderson et al., 2011). These pollen records are shown alongside summer insolation data for 37°N (Laskar et al., 2004). **(B)** Shallow-marine records from shelf-incised canyons in the Alboran Sea displaying variability in silt (%) and Ti/Ca and Fe/Ca ratios. These records are from sediment cores VC08 (Motril Canyon) and GC35 (Calahonda Canyon). **(C)** Deep-marine records from the Alboran Sea basin displaying variability in Ti/Ca ratio. These records are from sediment cores TTR-12_292G and TTR-17_434G (Mesa-Fernández et al., 2022). North Atlantic Oscillation (NAO) index (reversed) from a climate proxy reconstruction from Greenland (Olsen et al., 2012) is also plotted for comparison. The inset map shows the sediment core locations in the southern Iberian Peninsula. Abbreviations include IRHP (Iberian Roman Humid Period), DA (Dark Ages), MCA (Medieval Climate Anomaly), LIA (Little Ice Age), IP (Industrial Period). Yellow dashed lines indicate more arid intervals, while the blue shaded area highlights a wet period. The grey dashed line indicates the beginning of the Industrial Period.

from the southwestern Iberian margin, such as the Tagus Basin (e.g., Vis et al., 2016; Gomes et al., 2020).

The comparison of sediment records from continental, shallow and deep marine environments is inherently complex. However, the observed increase in detrital inputs in the Sierra Nevada wetland records, as well as in shallow and deep marine sedimentary records (Figure 8), provides compelling evidence of source-to-sink coupling between terrestrial, shelf, and slope environments. The Motril Canyon, which primarily functioned as a sediment trap, serves as a key site for understanding this linkage. Multi-proxy evidence from this site indicates that sediment flux to the marine environment has risen over the past 2000 years (Figure 3), with intensified human activities amplifying erosion rates and sediment fluxes. While the Motril Canyon primarily operated as a river-fed system and may not have served as a direct conduit between fluvial and deepwater systems, it nonetheless offers clear evidence of sediment transfer from the continent to the shallow shelf (Figure 8). A net transfer of detrital sediments from the shelf to the slope and ultimately to deeper marine settings likely occurred through turbidity currents. Sediment retention in littoral cells, combined with downslope transport via longshore drift-fed systems—such as the Carchuna and Calahonda canyon systems—may have facilitated the transfer of sediments from the shallow shelf to the slope. The marked increase in detrital input observed in deep marine records from the Alboran basin at ~1500 years BP (Figure 8) supports this interpretation, indicating that sediments were ultimately transported to deeper marine environments. This interconnectedness between the shelf and slope environments is evident, even though the Motril Canyon itself did not directly channeled sediments to the deep sea.

The increase in terrigenous input over the last 2000 years CE cannot be attributed solely to climatic factors. Instead, land use intensification in southern Iberia, including deforestation, agricultural expansion and mining, have likely amplified erosional processes and enhanced sediment fluxes to both shallow and deep marine environments (e.g., Davis et al., 2000; Boone and Worman, 2007; Delgado et al., 2012; Vis et al., 2016; Hanebuth et al., 2018; Gomes et al., 2020; Mesa-Fernández et al., 2022), complicating the interpretation of purely climatic signals. As a result, paleoclimate reconstructions spanning the last 2000 years that rely on elemental geochemical ratios must consider the potential overprinting of climatic signatures by human-induced impacts.

6 Conclusion

- 1) The recent sedimentary infillings of the Motril, Carchuna, and Calahonda submarine canyons exhibit distinct characteristics, shaped by differing sources and sediment transport mechanisms. The Motril Canyon primarily functioned as a river-fed system, influenced by fluvial discharges from the Guadalfeo River during periods of calm hydrodynamic conditions. As a highly effective sediment trap, it preserves a detailed sedimentary record that enables the reconstruction of both natural and human-induced paleoenvironmental changes during the Late Holocene. In contrast, the Carchuna Canyon is dominated by a longshore-drift-fed system, where wave focusing and high shear stress at the canyon head mobilized coarse-grained sediments which were eventually transported
- 2) The Motril Canyon provides the most continuous and well-preserved sedimentary record for the last ~2000 years. This record is characterized by four stages that largely correspond to historical climatic periods and are marked by changes in sediment production. During the Iberian Roman Humid Period (2600–1600 cal. yr BP), terrigenous sediment input reduced, likely due to limited Guadalfeo River discharges, despite a final humid phase. The Dark Ages (1500–1000 cal. yr BP) witnessed a progressive transition from coarse-to fine-grained sedimentation, with increased rates indicating higher terrigenous input, driven by widespread soil erosion and land degradation under moderate rainfall conditions. These conditions persisted during the Medieval Climate Anomaly (1050–650 cal. yr BP), with high sedimentation rates and land-use-driven increases in sediment flux, though without clear evidence of rainfall patterns. The Little Ice Age (650–150 cal. yr BP) was marked by a high rate of fine-grained sediment deposition, linked to increased rainfall and human activity, while the Industrial Period (150 cal. yr BP–present) has been characterized by a general decrease in fluvial-derived material, suggesting a shift to drier conditions.
- 3) The increase in terrigenous input over the last 2000 years cannot be solely attributed to climatic variability. Instead, anthropogenic activities have significantly amplified erosion rates and sediment fluxes into marine basins, complicating the interpretation of purely climate-driven sedimentary signals. The contrasting depositional dynamics of the Motril Canyon, which acted as a sediment trap, and the more dynamic transport systems of the Carchuna and Calahonda canyons, highlight the complexity of source-to-sink systems in this region. These findings underscore the necessity of integrating sedimentary records from multiple depositional environments to accurately reconstruct paleoenvironmental changes.

Data availability statement

The raw data supporting the conclusions of this article will be made available by the authors, without undue reservation.

Author contributions

AL-Q: Conceptualization, Formal Analysis, Investigation, Methodology, Resources, Software, Visualization, Writing – original draft, Writing – review and editing. ÁP-B: Conceptualization, Investigation, Visualization, Writing – original draft, Writing – review and editing, Data curation, Methodology, Project administration, Supervision, Validation. FJL: Conceptualization, Data curation, Funding acquisition, Investigation, Project administration, Resources, Supervision, Validation, Writing – original draft, Writing – review and editing, Methodology. ER-C: Investigation, Methodology, Visualization, Writing – original draft, Writing – review and editing, Formal Analysis, Software.

JC-E: Formal Analysis, Investigation, Visualization, Writing – original draft, Writing – review and editing, Conceptualization. JNP-A: Investigation, Resources, Visualization, Writing – original draft, Writing – review and editing, Formal Analysis. IM: Resources, Writing – original draft, Writing – review and editing, Investigation, Visualization. AM: Formal Analysis, Methodology, Software, Writing – original draft, Writing – review and editing, Resources, Validation. NP-P: Formal Analysis, Methodology, Writing – original draft, Writing – review and editing. TA-P: Formal Analysis, Methodology, Writing – original draft, Writing – review and editing. LW: Formal Analysis, Methodology, Writing – original draft, Writing – review and editing.

Funding

The author(s) declare that financial support was received for the research and/or publication of this article. This research was funded by the projects Alboran Shelf-Slope cOUpling processes and deep sediMent trAnsfEr: Source To Sink approaches and implications for biodiversity-ALSSOMAR S2S (CTM2017-88237P) (Ministerio de Economía y Competitividad, Spanish government), and Sediment gravity flows and Anthropogenic Impacts in a MEDiterranean deltaic-and-canyon environment: Causal relationships and consequences-SANIMED (PID2021-125489OB-I00) funded by MCIN/AEI/10.13039/501100011033/FEDER (Ministerio de Ciencia e Innovación, Spanish government). AL-Q also thanks the Spanish Ministry of Science and Innovation (MCIN) for Research Contract FJC 2021-047046-I (MCIN/AEI/10.13039/501100011033 and NextGenerationEU/PRTR). IM also acknowledge the financial support of the Portuguese Foundation for Science and Technology (FCT) for the contract CEECINST/00052/2021/CP2792/CT0012, and the projects CIMA (UID/0350/2020), and ARNET (LA/P/0069/2020). ER-C is also grateful to the Spanish Ministry of Education and Vocational Training for awarding her a Collaboration Grant to work at the University of Granada's Department of Stratigraphy and Paleontology. Finally, AL-Q, AP-B, JNP-A and NP-P thanks the Research Group RNM-190 ANALISIS DE CUENCAS (Junta de Andalucía).

References

- Abrantes, F., Lebreiro, S., Rodrigues, T., Gil, I., Bartels-Jónsdóttir, H., Oliveira, P., et al. (2005). Shallow-marine sediment cores record climate variability and earthquake activity off Lisbon (Portugal) for the last 2000 years. *Quat. Sci. Rev.* 24, 2477–2494. doi:10.1016/j.quascirev.2004.04.009
- Aiello, G., Iorio, M., Molisso, F., and Sacchi, M. (2020). Integrated Morpho-Bathymetric, seismic-stratigraphic, and sedimentological data on the Dohrn Canyon (Naples Bay, Southern Tyrrhenian Sea): relationships with volcanism and tectonics. *Geosciences* 10, 319. doi:10.3390/geosciences10080319
- Aldaya, F. (1981). *Mapa geológico y memoria explicativa de la Hoja 1056 (Albuñol) del Mapa Geológico de España*. Madrid: IGME.
- Aldaya, F., García-Duenas, V., and Navarro-Vila, F. (1979). Los mantos alpujarrides del tercio central de las cordilleras deticas. Ensayo de la correlacion tectonica de los alpujarrides. *Acta Geol. Hisp.* 14 (1), 154–166.
- Álvarez-Martí-Aguilar, M. (2022). “Earthquakes and tsunamis in Ancient iberia: the historical sources. In historical earthquakes, tsunamis and archaeology in the iberian peninsula,” in *Natural science in archaeology*. Singapore: Springer, 37–62. doi:10.1007/978-981-19-1979-4
- Amblas, D., Ceramicola, S., Gerber, T. P., Canals, M., Chiocci, F. L., Dowdeswell, J. A., et al. (2018). “Submarine canyons and gullies,” in *Submarine geomorphology*. Editors A. Micallef, S. Krastel, and A. Savini (Cham: Springer Geol. Springer), 251–272.
- Anderson, R. S., Jiménez-Moreno, G., Carrión, J. S., and Pérez-Martínez, C. (2011). Postglacial history of alpine vegetation, fire, and climate from Laguna de Río Seco, Sierra Nevada, southern Spain. *Quat. Sci. Rev.* 30, 1615–1629. doi:10.1016/j.quascirev.2011.03.005
- Anthony, E. J., Marriner, N., and Morhange, C. (2014). Human influence and the changing geomorphology of Mediterranean deltas and coasts over the last 6000 years: from progradation to destruction phase? *Earth-Science Rev.* 139, 336–361. doi:10.1016/j.earscirev.2014.10.003
- Ausín, B., Flores, J. A., Sierro, E.-J., Bárcena, M.-A., Hernández-Almeida, I., Francés, G., et al. (2015). Coccolithophore productivity and surface water dynamics in the Alboran Sea during the last 25kyr. *Palaeogeogr. Palaeoclimatol. Palaeoecol.* 418, 126–140. doi:10.1016/j.palaeo.2014.11.011
- Babonneau, N., Savoye, B., Cremer, M., and Klein, B. (2002). Morphology and architecture of the present canyon and channel system of the Zaire deep-sea fan. *Mar. Pet. Geol.* 19 (4), 445–467. doi:10.1016/s0264-8172(02)00009-0

Acknowledgments

The authors thank the captain and crew of R/V Sarmiento de Gamboa for their dedication and constant support for the execution of activities onboard, and to the participants of the ALSSOMAR oceanographic expedition for their help during sediment core acquisition.

Conflict of interest

The authors declare that the research was conducted in the absence of any commercial or financial relationships that could be construed as a potential conflict of interest.

The author(s) declared that they were an editorial board member of Frontiers, at the time of submission. This had no impact on the peer review process and the final decision.

Generative AI statement

The author(s) declare that no Generative AI was used in the creation of this manuscript.

Publisher's note

All claims expressed in this article are solely those of the authors and do not necessarily represent those of their affiliated organizations, or those of the publisher, the editors and the reviewers. Any product that may be evaluated in this article, or claim that may be made by its manufacturer, is not guaranteed or endorsed by the publisher.

Supplementary material

The Supplementary Material for this article can be found online at: <https://www.frontiersin.org/articles/10.3389/feart.2025.1597056/full#supplementary-material>

- Bahr, A., Jiménez-Espejo, F. J., Kolasinac, N., Grunert, P., Hernández-Molina, F. J., Rohl, U., et al. (2014). Deciphering bottom current velocity and paleoclimate signals from contourite deposits in the Gulf of Cádiz during the last 140 kyr: an inorganic geochemical approach. *Geochem. Geophys. Geosyst.* 15, 3145–3160. doi:10.1002/2014GC005356
- Ballesteros, M., Rivera, J., Muñoz, A., Muñoz-Martín, A., Acosta, J., Carbó, A., et al. (2008). Alboran Basin, southern Spain-part II: neogene tectonic implications for the orogenic float model. *Mar. Pet. Geol.* 25 (1), 75–101. doi:10.1016/j.marpetgeo.2007.05.004
- Bárceñas, P. (2013). Procesos morfogenéticos y evolución reciente de los depósitos prodeltaicos del sureste de la península ibérica: aplicaciones de modelos matemáticos. Ph.D. Thesis Doctoral. Malaga, Spain: University of Malaga.
- Bárceñas, P., Lobo, F. J., Fernández-Salas, L. M., Mendes, I., López-González, N., and Macías, J. (2024). The late holocene evolution of the adra delta subaqueous system (Northern Alboran Sea): seismic-stratigraphic and geomorphic evidence of millennial scale climatic and anthropic effects. *Mar. Geol.* 477, 107386. doi:10.1016/j.margeo.2024.107386
- Bárceñas, P., Lobo, F. J., Macías, J., Fernández-Salas, L. M., and Díaz del Río, V. (2011). Spatial variability of surficial sediments on the northern shelf of the Alboran Sea: the effects of hydrodynamic forcing and supply of sediment by rivers. *J. Iber. Geol.* 37 (2), 195–214. doi:10.5209/rev_jige.2011.v37.n2.8
- Bard, E., Tuna, T., Fagault, Y., Bonvalot, L., Wacker, L., Fahrni, S., et al. (2015). AixMICADAS, the accelerator mass spectrometer dedicated to ¹⁴C recently installed in Aix-en-Provence, France. *Nucl. Instrum. Methods Phys. Res. Sect. B-Beam Interact. Mater. Atoms* 361, 80–86. doi:10.1016/j.nimb.2015.01.075
- Bartels-Jónsdóttir, H. B., Knudsen, K. L., Abrantes, F., Lebreiro, S., and Eiriksson, J. (2006). Climate variability during the last 2000 years in the Tagus Prodelt, western Iberian Margin: benthic Foraminifera and stable isotopes. *Mar. Micropaleontol.* 59, 83–103. doi:10.1016/j.marmicro.2006.01.002
- Bartels-Jónsdóttir, H. B., Voelker, A. H. L., Abrantes, F. G., Salgueiro, E., Rodrigues, T., and Knudsen, K. L. (2015). High-frequency surface water changes in the Tagus prodelta off Lisbon, eastern North Atlantic, during the last two millennia. *Mar. Micropaleontol.* 117, 13–24. doi:10.1016/j.marmicro.2015.03.001
- Bassetti, M., Berné, S., Sicre, M. A., Dennielou, B., Alonso, Y., Buscail, R., et al. (2016). Holocene hydrological changes in the Rhône River (NW Mediterranean) as recorded in the marine mud belt. *Clim. Past.* 12, 1539–1553. doi:10.5194/cp-12-1539-2016
- Benito, G., Macklin, M. G., Panin, A., Rossato, S., Fontana, A., Jones, A. F., et al. (2015). Recurring flood distribution patterns related to short-term holocene climatic variability. *Sci. Rep.* 5, 16398. doi:10.1038/srep16398
- Benito, G., Thorndyraft, V. R., Rico, M., Sánchez-Moya, Y., and Sopena, A. (2008). Palaeoflood and floodplain records from Spain: evidence for long-term climate variability and environmental changes. *Geomorphology* 101, 68–77. doi:10.1016/j.geomorph.2008.05.020
- Bernárdez, P., González-Álvarez, R., Francés, G., Prego, R., Bárcena, M. A., and Romero, O. E. (2008). Late holocene history of the rainfall in the NW Iberian Peninsula-evidence from a marine record. *J. Mar. Syst.* 72, 366–382. doi:10.1016/j.jmarsys.2007.03.009
- Bernhardt, A., and Schwanghart, W. (2021). Where and why do submarine canyons remain connected to the shore during sea-level rise? Insights from global topographic analysis and Bayesian regression. *Geophys. Res. Lett.* 48 (10), e2020GL092234. doi:10.1029/2020gl092234
- Bini, M., Zanchetta, G., Regattieri, E., Isola, I., Drysdale, N., Fabiani, F., et al. (2020). Hydrological changes during the Roman Climatic Optimum in northern Tuscany (Central Italy) as evidenced by speleothem records and archaeological data. *J. Quat. Sci.* 1–12. doi:10.1002/jqs.3224
- Blott, S. J., and Pye, K. (2001). Gradstat: a grain size distribution and statistics package for the analysis of unconsolidated sediments. *Earth Surf. Process. Landforms* 26, 1237–1248. doi:10.1002/esp.261
- Boone, J. L., and Worman, F. S. (2007). Rural settlement and soil erosion from the late Roman Period through the medieval Islamic Period in the lower Alentejo of Portugal. *J. Field Archaeol.* 32, 115–132. doi:10.1179/009346907791071665
- Bosman, A., Romagnoli, C., Madricardo, F., Correggiari, A., Remia, A., Zubalich, R., et al. (2020). Short-term evolution of Po della Pila delta lobe from time lapse high-resolution multibeam bathymetry (2013–2016). *Estuar. Coast. Shelf Sci.* 233, 106533. doi:10.1016/j.ecss.2019.106533
- Boudreau, B. P. (1998). Mean mixed depth of sediments: the wherefore and the why. *Limnol. Oceanogr.* 43 (3), 524–526. doi:10.4319/lo.1998.43.3.0524
- Bouimetarhan, I., Groeneveld, J., Dupont, L., and Zonneveld, K. (2013). Low-to high-productivity pattern within Heinrich Stadial 1: inferences from dinoflagellate cyst records off Senegal. *Glob. Planet. Chang.* 106, 64–76. doi:10.1016/j.gloplacha.2013.03.007
- Bowman, S. (1990). *Radiocarbon dating*. Berkeley: British Museum.
- Brankart, J. M., and Pinardi, N. (2001). Abrupt cooling of the mediterranean levantine intermediate water at the beginning of the 1980s: observational evidence and model simulation. *J. Phys. Oceanogr.* 31 (8), 2307–2320. doi:10.1175/1520-0485(2001)031<2307:acotml>2.0.co;2
- Brothers, D. S., Brink, U. S., Andrews, B. D., and Chaytor, J. D. (2013). Geomorphic characterization of the U.S. Atlantic continental margin. *Mar. Geol.* 338, 46–63. doi:10.1016/j.margeo.2012.12.008
- Budillon, F., Senatore, M. R., Insinga, D. D., Iorio, M., Lubritto, C., Roca, M., et al. (2012). Late Holocene sedimentary changes in shallow water settings: the case of the Sele River offshore in the Salerno Gulf (south-eastern Tyrrhenian Sea, Italy). *Rendiconti Lincei* 23, 25–43. doi:10.1007/s12210-012-0164-6
- Caley, T., Malaizé, B., Zaragosi, S., Rossignol, L., Bourget, J., Eynaud, F., et al. (2011). New Arabian Sea records help decipher orbital timing of Indo-Asian monsoon. *Earth Planet. Sci. Lett.* 308, 433–444. doi:10.1016/j.epsl.2011.06.019
- Camerlenghi, A., Del Ben, A., Hübscher, C., Forlin, E., Geletti, R., Brancatelli, G., et al. (2020). Seismic markers of the messinian salinity crisis in the deep Ionian Basin. *Basin Res.* 32, 716–738. doi:10.1111/bre.12392
- Camuera, J., Jiménez-Moreno, G., Ramos-Román, M. J., García-Alix, A., Toney, J. L., Anderson, R. S., et al. (2018). Orbital-scale environmental and climatic changes recorded in a new ~ 200,000-year-long multiproxy sedimentary record from Padul, southern Iberian Peninsula. *Quat. Sci. Rev.* 198, 91–114. doi:10.1016/j.quascirev.2018.08.014
- Canals, M., Casamor, J. L., Lastras, G., Monaco, A., Acosta, J., Berné, S., et al. (2004). The role of canyons on strata formation. *Oceanography* 17 (4), 80–91. doi:10.5670/oceanog.2004.06
- Canals, M., Puig, P., De Madron, X. D., Heussner, S., Palanques, A., and Fabres, J. (2006). Flushing submarine canyons. *Nature* 444, 354–357. doi:10.1038/nature05271
- Carrión, J. S. (2002). Patterns and processes of late quaternary environmental change in a montane region of southwestern Europe. *Quat. Sci. Rev.* 21, 2047–2066. doi:10.1016/s0277-3791(02)00010-0
- Carson, B., Baker, E. T., Hickey, B. M., Nittrouer, C. A., De Master, D. J., Thorbjarnarson, K. W., et al. (1986). Modern sediment dispersal and accumulation in quinnault submarine canyon - a summary. *Mar. Geol.* 71, 1–13. doi:10.1016/0025-3227(86)90030-7
- Cerrillo-Escoriza, J., Lobo, F. J., Puga-Bernabéu, Á., Bárceñas, P., Mendes, I., Pérez-Asensio, J. N., et al. (2024a). Variable downcanyon morphology controlling the recent activity of shelf-incised submarine canyons (Alboran Sea, western mediterranean). *Geomorphology* 453, 109127. doi:10.1016/j.geomorph.2024.109127
- Cerrillo-Escoriza, J., Micallef, A., Lobo, F. J., Puga-Bernabéu, Á., Bárceñas, P., Schulten, I., et al. (2024b). Bedform development in confined and unconfined settings of the Carchuna Canyon (Alboran Sea, western Mediterranean Sea): an example of cyclic steps in shelf-incised canyons. *Mar. Geol.* 478, 107429. doi:10.1016/j.margeo.2024.107429
- Cerrillo-Escoriza, J., Lobo, F. J., Puga-Bernabéu, Á., Rueda, J. L., Bárceñas, P., Sánchez-Guillamón, O., et al. (2023). Origin and driving mechanisms of marine litter in the shelf-incised Motril, Carchuna, and Calahonda canyons (northern Alboran Sea). *Front. Mar. Sci.* 10, 1–24. doi:10.3389/fmars.2023.1098927
- Chawchai, S., Kylander, M. E., Chabangborn, A., Lowemark, L., and Wohlfarth, B. (2016). Testing commonly used X-ray fluorescence core scanning-based proxies for organic rich lake sediments and peat. *Boreas* 45 (1), 180–189. doi:10.1111/bor.12145
- Cita, M. B., Wright, R. C., Ryan, W. B. F., and Longinelli, A. (1978). Messinian paleoenvironments. Initial rep. Deep Sea Drill. *Proj.* 42A, 1003–1035.
- Comas, M. C., Platt, J. P., Soto, J. L., and Watts, A. B. (1999). The origin and tectonic history of the Alboran Basin: insights from leg 161 results. *Proc. Ocean. Drill. Program Sci. Results* 161, 555–579. doi:10.2973/odp.proc.sr.161.262.1999
- Combourieu-Nebout, N., Peyron, O., Dormoy, I., Desprat, S., Beaudouin, C., Kotthoff, U., et al. (2009). Rapid climatic variability in the West Mediterranean during the last 25 000 years from high resolution pollen data. *Clim. Past.* 5, 503–521. doi:10.5194/cp-5-503-2009
- Covault, J. A., and Graham, S. A. (2010). Submarine fans at all sea-level stands: tectono-morphologic and climatic controls on terrigenous sediment delivery to the deep sea. *Geology* 38 (10), 939–942. doi:10.1130/g31081.1
- Croudace, I. W., Rindby, A., and Rothwell, R. G. (2006). "ITRAX: description and evaluation of a new multi-function X-ray core scanner," in *New techniques in sediment core analysis*. Editor R. G. Rothwell, 51–63. London, UK: Geol. Soc. of London. doi:10.1144/GSL.SP.2006.267.01.04
- Davis, Jr., R. A., Welty, A. T., Borrego, J., Morales, J. A., Pendon, J. G., and Ryan, J. G. (2000). Rio Tinto estuary (Spain): 5000 years of pollution. *Environ. Geol.* 39, 1107–1116. doi:10.1007/s002549900096
- Delgado, J., Boski, T., Nieto, J. M., Pereira, L., Moura, D., Gomes, A., et al. (2012). Sea-level rise and anthropogenic activities recorded in the late Pleistocene/Holocene sedimentary infill of the Guadiana Estuary (SW Iberia). *Quat. Sci. Rev.* 33, 121–141. doi:10.1016/j.quascirev.2011.12.002
- de Mahiques, M. M., Wainer, I. K. C., Burone, L., Nagai, R., Sousa, S. H. M., Figueira, R. C. L., et al. (2009). A high-resolution Holocene record on the Southern Brazilian shelf: paleoenvironmental implications. *Quat. Int.* 206, 52–61. doi:10.1016/j.quaint.2008.09.010
- Dickson, A. J., Leng, M. J., Maslin, M. A., and Rohl, U. (2010). Oceanic, atmospheric and ice-sheet forcing of South East Atlantic Ocean productivity and

- South African monsoon intensity during MIS-12 to 10. *Quat. Sci. Rev.* 29, 3936–3947. doi:10.1016/j.quascirev.2010.09.014
- Díez-Herrero, A., Mateos, R. M., Vázquez-Tarrio, D., López-Marcos, A., and Brao-González, y F. J. (2024). One catastrophic flood every millennium: synchronicity of extreme floods and global warm periods in the multi-archive record of the roman theatre of Guadix (Granada, SE Spain). *Glob. Planet. Change* 233, 104363. doi:10.1016/j.gloplacha.2024.104363
- Do Couto, D., Gorini, C., Jolivet, L., Lebret, N., Augier, R., Gumiaux, C., et al. (2016). Tectonic and stratigraphic evolution of the Western Alboran Sea Basin in the last 25 Myrs. *Tectonophysics* 677–678, 280–311. doi:10.1016/j.tecto.2016.03.020
- Durand, M., Mojtahid, M., Maillat, G. M., Baltzer, A., Schmidt, S., Blet, S., et al. (2018). Late Holocene record from a Loire River incised paleovalley (French inner continental shelf): insights into regional and global forcing factors. *Palaeogeogr. Palaeoclimatol. Palaeoecol.* 511, 12–28. doi:10.1016/j.palaeo.2018.06.035
- Ercilla, G., Juan, C., Periañez, R., Alonso, B., Abril, J. M., Estrada, F., et al. (2019). Influence of along slope processes on modern turbidite systems and canyons in the Alboran Sea (southwestern Mediterranean). *Deep. Res. Part I Oceanogr. Res. Pap.* 144, 1–16. doi:10.1016/j.dsr.2018.12.002
- Evangelinos, D., Escutia, C., Etourneau, J., Hoem, F., Bijl, P. K., Boterblom, W., et al. (2020). Late oligocene-miocene proto-antarctic Circumpolar Current dynamics off the Wilkes Land margin, East Antarctica. *Glob. Planet. Change* 191, 103221. doi:10.1016/j.gloplacha.2020.103221
- Fernández-Salas, L. M., Dabrio, C. J., Goy, J. L., Díaz del Río, V., Zazo, C., Lobo, F. J., et al. (2009). Land-sea correlation between late Holocene coastal and infralittoral deposits in the SE Iberian Peninsula (Western Mediterranean). *Geomorphology* 104, 4–11. doi:10.1016/j.geomorph.2008.05.013
- Fisher, W. L., Galloway, W. E., Steel, R. J., Olariu, C., Kerans, C., and Mohrig, D. (2021). Deep-water depositional systems supplied by shelf-incising submarine canyons: recognition and significance in the geologic record. *Earth Sci. Rev.* 214, 103531. doi:10.1016/j.earscirev.2021.103531
- Fletcher, W. J., Debret, M., and Goñi, M. F. S. (2013). Mid-holocene emergence of a low-frequency millennial oscillation in western Mediterranean climate: implications for past dynamics of the North Atlantic atmospheric westerlies. *Holocene* 23, 153–166. doi:10.1177/0959683612460783
- Fletcher, W. J., and Sánchez-Goñi, M. F. (2008). Orbital- and sub-orbital-scale climate impacts on vegetation of the western Mediterranean basin over the last 48,000 yr. *Quat. Res.* 70, 451–464. doi:10.1016/j.yqres.2008.07.002
- Foglini, F., Rovere, M., Tonielli, R., Castellan, G., Prampolini, M., Budillon, F., et al. (2025). A new multi-grid bathymetric dataset of the Gulf of Naples (Italy) from complementary multi-beam echo sounders. *Earth Syst. Sci. Data* 17 (1), 181–203. doi:10.5194/essd-17-181-2025
- Folk, R. L., and Ward, W. C. (1957). Brazos River bar: a study in the significance of grain size parameters. *J. Sediment. Petrol.* 27, 3–26. doi:10.1306/74d70646-2b21-11d7-8648000102c1865d
- Fouinat, L., Sabatier, P., Poulencar, J., Reyss, J.-L., Montet, X., and Arnaud, F. (2017). A new CT scan methodology to characterize a small aggregation gravel clast contained in a soft sediment matrix. *Earth Surf. Dynam.* 5, 199–209. doi:10.5194/esurf-5-199-2017
- Frey-Martinez, J., Cartwright, J. A., and Burgess, P. M. (2004). “3D seismic interpretation of the Messinian unconformity in the Valencia, Spain,” in *3D seismic technology: application to the exploration of sedimentary basins*. Editors R. J. Davies, J. A. Cartwright, S. A. Stewart, M. Lappin, and R. Underhill (London: Geol Soc. Mem.), 91–100.
- Gallego, M. C., Trigo, R. M., Vaquero, J. M., Brunet, M., García, J. A., Sigró, J., et al. (2011). Trends in frequency indices of daily precipitation over the Iberian Peninsula during the last century. *J. Geophys. Res. Atmos.* 116, D02109. doi:10.1029/2010jd014255
- Gao, S., and Collins, M. B. (2014). Holocene sedimentary systems on continental shelves. *Mar. Geol.* 352, 268–294. doi:10.1016/j.margeo.2014.03.021
- García-Alix, A., Jiménez-Espejo, F. J., Jiménez-Moreno, G., Toney, J. L., Ramos-Román, M. J., Camuera, J., et al. (2018). Holocene geochemical footprint from semi-arid alpine wetlands in southern Spain. *Sci. Data* 5, 180024. doi:10.1038/sdata.2018.24
- García-Alix, A., Jiménez-Espejo, F. J., Lozano, J. A., Jiménez-Moreno, G., Martínez-Ruiz, F., García Sanjuán, L., et al. (2013). Anthropogenic impact and lead pollution throughout the Holocene in Southern Iberia. *Sci. Total Environ.* 449, 451–460. doi:10.1016/j.scitotenv.2013.01.081
- García-Alix, A., Jiménez-Espejo, F. J., Toney, J. L., Jiménez-Moreno, G., Ramos-Román, M. J., Anderson, R. S., et al. (2017). Alpine bogs of southern Spain show human-induced environmental change superimposed on long-term natural variations. *Sci. Rep.* 7, 7439. doi:10.1038/s41598-017-07854-w
- García-Lafuente, J., Cano, N., Vargas, M., Rubín, J. P., and Hernandez-Guerra, A. (1998). Evolution of the Alboran Sea hydrographic structures during July 1993. *Deep Sea Res Part I: Oceanogr. Res. Pap.* 45 (1), 39–65. doi:10.1016/s0967-0637(97)00216-1
- García-Ruiz, J. M. (2010). The effects of land uses on soil erosion in Spain: a review. *Catena* 81, 1–11. doi:10.1016/j.catena.2010.01.001
- GEBCO (2023). General bathymetric chart of the oceans (GEBCO). Available online at: <https://www.gebco.net>. (Accessed August 5, 2023)
- Goldfinger, C., Ikeda, Y., Yeats, R. S., and Ren, J. (2013). Superquakes and supercycles. *Seismol. Res. Lett.* 84 (1), 24–32. doi:10.1785/0220110135
- Goldfinger, C., Nelson, C. H., and Johnson, J. E. (2003). Holocene earthquake records from the Cascadia subduction zone and northern San Andreas Fault based on precise dating of offshore turbidites. *Annu. Rev. Earth Planet. Sci.* 31, 555–577. doi:10.1146/annurev.earth.31.100901.141246
- Goldfinger, C., Nelson, C. H., Morey, A. E., Johnson, J. E., Patton, J. R., Karabanov, E., et al. (2012). Turbidite event history—methods and implications for Holocene paleoseismicity of the Cascadia subductionzone. *U.S. Geol. Surv. Prof. Pap.* 1661–F, 170. doi:10.3133/pp1661F
- Gomes, S. D., Flectcher, W. J., Rodrigues, T., Stone, A., Abrantes, F., and Naughton, F. (2020). Time-transgressive Holocene maximum of temperate and Mediterranean forest development across the Iberian Peninsula reflects orbital forcing. *Palaeogeogr. Palaeoclimatol. Palaeoecology* 550, 1–16. doi:10.1016/j.palaeo.2020.109739
- Gómez de la Peña, L. R., Ranero, C., Gràcia, E., and Booth-Rea, G. (2021). The evolution of the westernmost Mediterranean basins. *Earth Sci. Rev.* 214, 103445. doi:10.1016/j.earscirev.2020.103445
- Gonzalez, R., Araújo, M. F., Burdloff, D., Cachão, M., Cascalho, J., Corredeira, C., et al. (2007). Sediment and pollutant transport in the Northern Gulf of Cadiz: a multi-proxy approach. *J. Mar. Syst.* 68, 1–23. doi:10.1016/j.jmarsys.2006.10.007
- Granata, T. C., Vidondo, B., Duarte, C. M., Satta, M. P., and Gracia, M. (1999). Hydrodynamics and particle transport associated with a submarine canyon off Blanes (Spain), NW Mediterranean Sea. *Cont. Shelf Res.* 19, 1249–1263. doi:10.1016/s0278-4343(98)00118-6
- Grove, C. A., Nagtegaal, R., Zinke, J., Scheufen, T., Koster, B., Kasper, S., et al. (2010). River runoff reconstructions from novel spectral luminescence scanning of massive coral skeletons. *Coral Reefs* 29, 579–591. doi:10.1007/s00338-010-0629-y
- Hammer, Ø., Harper, D. A. T., and Ryan, P. D. (2001). PAST: paleontological statistics software package for education and data analysis. *Palaeontol. Electron.* 4, 9.
- Hanebuth, T. J. J., King, M. L., Mendes, I., Lebreiro, S., Lobo, F. J., Oberle, F. K., et al. (2018). Hazard potential of widespread but hidden historic offshore heavy metal (Pb, Zn) contamination (Gulf of Cadiz, Spain). *Sci. Total Environ.* 637–638, 561–576. doi:10.1016/j.scitotenv.2018.04.352
- Harris, P., Macmillan-Lawler, M., Rupp, J., and Baker, E. (2014). Geomorphology of the oceans. *Mar. Geol.* 352, 4–24. doi:10.1016/j.margeo.2014.01.011
- Harris, P. T., and Whiteway, T. (2011). Global distribution of large submarine canyons: geomorphic differences between active and passive continental margins. *Mar. Geol.* 285, 69–86. doi:10.1016/j.margeo.2011.05.008
- Heaton, T. J., Köhler, P., Butzin, M., Bard, E., Reimer, R. W., Austin, W. E. N., et al. (2020). Marine20 - the marine radiocarbon age calibration curve (0–55,000 cal BP). *Radiocarbon* 62 (4), 779–820. doi:10.1017/rdc.2020.68
- Helama, S., Jones, P. D., and Briffa, K. R. (2017). Dark ages cold period: a literature review and directions for future research. *Holocene* 27, 1600–1606. doi:10.1177/0959683617693898
- Hillaire-Marcel, C., and De Vernal, A. (2007). *Proxies in late Cenozoic paleoceanography*. Amsterdam: Elsevier.
- Hodell, D. A., Channell, J. E. T., Curtis, J. H., Romero, O. E., and Röhl, U. (2008). Onset of “hudson strait” heinrich events in the eastern North Atlantic at the end of the middle pleistocene transition (~640 ka)? *Paleoceanography* 23, PA4218. doi:10.1029/2008pa001591
- Hsü, K. J., Montadert, L., Bernoulli, D., Cita, M. B., Erickson, A., Garrison, R. E., et al. (1977). History of the Mediterranean salinity crisis. *Nature* 267, 399–403. doi:10.1038/267399a0
- Jabaloy-Sánchez, A., Lobo, F. J., Azor, A., Bárcenas, P., Fernández-Salas, L. M., del Río, V. D., et al. (2010). Human-driven coastline changes in the Adra River deltaic system, southeast Spain. *Geomorphology* 119, 9–22. doi:10.1016/j.geomorph.2010.02.004
- Jabaloy-Sánchez, A., Lobo, F. J., Azor, A., Bárcenas, P., Fernández-Salas, L. M., del Río, V. D., et al. (2014). Six thousand years of coastline evolution in the Guadalfeo deltaic system (southern Iberian Peninsula). *Geomorphology* 206, 374–391. doi:10.1016/j.geomorph.2013.08.037
- Jiménez-Espejo, F. J., Martínez-Ruiz, F., Rogerson, M., González-Donoso, J. M., Romero, O., Linares, D., et al. (2008). Detrital input, productivity fluctuations, and water mass circulation in the westernmost Mediterranean Sea since the last glacial maximum. *Geochem. Geophys. Geosy.* 9, Q11U02. doi:10.1029/2008GC002096
- Jiménez-Moreno, G., and Anderson, R. S. (2012). Holocene vegetation and climate change recorded in alpine bog sediments from the Borreguiles de la Virgen, Sierra Nevada, southern Spain. *Quat. Res.* 77, 44–53. doi:10.1016/j.yqres.2011.09.006
- Jiménez-Moreno, G., García-Alix, A., Hernández-Corbalán, M. D., Anderson, R. S., and Delgado-Huertas, A. (2013). Vegetation, fire, climate and human disturbance history in the southwestern Mediterranean area during the late Holocene. *Quat. Res.* 79, 110–122. doi:10.1016/j.yqres.2012.11.008
- Juan, C., Ercilla, G., Javier Hernandez-Molina, F., Estrada, F., Alonso, B., Casas, D., et al. (2016). Seismic evidence of current-controlled sedimentation in the Alboran Sea during the Pliocene and Quaternary: palaeoceanographic implications. *Mar. Geol.* 378, 292–311. doi:10.1016/j.margeo.2016.01.006

- Khripounoff, A., Crassous, P., Lo Bue, N., Dennielou, B., and Silva Jacinto, R. (2012). Different types of sediment gravity flows detected in the Var submarine canyon (northwestern Mediterranean Sea). *Prog. Oceanogr.* 106, 138–153. doi:10.1016/j.pocan.2012.09.001
- Khripounoff, A., Vangriesheim, A., Crassous, P., and Etoubleau, J. (2009). High frequency of sediment gravity flow events in the Var submarine canyon (Mediterranean Sea). *Mar. Geol.* 263, 1–6. doi:10.1016/j.margeo.2009.03.014
- Kim, J., Wright, D. K., Hwang, J., Kim, J., and Oh, Y. (2019). The old wood effect revisited: a comparison of radiocarbon dates of wood charcoal and short-lived taxa from Korea. *Archaeol. Anthropol. Sci.* 11, 3435–3448. doi:10.1007/s12520-018-0766-8
- Lario, J., Zazo, C., and Goy, J. L. (1999). Fases de programación y evolución morfosedimentaria de la flecha litoral de Calahonda (Granada) durante el Holoceno. *Estud. Geol.* 55, 247–250. doi:10.3989/egool.99555-6164
- Lario, J., Zazo, C., Goy, J. L., Silva, P. G., Bardaji, T., Cabero, A., et al. (2011). Holocene palaeotsunami catalogue of SW Iberia. *Quat. Int.* 242 (1), 196–200. doi:10.1016/j.quaint.2011.01.036
- Laskar, J., Robutel, P., Joutel, F., Gastineau, M., Correia, A. C. M., and Levrard, B. (2004). A long term numerical solution for the insolation quantities of the Earth. *Astron. Astrophys. Nor.* 428, 261–285. doi:10.1051/0004-6361:20041335
- Leblanc, M., Morales, J. A., Borrego, J., and Elbaz-Poulichet, F. (2000). 4,500-year-old mining pollution in southwestern Spain: long-term implications for modern mining pollution. *Econ. Geol.* 95, 655–662. doi:10.2113/gsecongeo.95.3.655
- Lebreiro, S. M., Francés, G., Abrantes, F. F. G., Diz, P., Bartels-Jónsdóttir, H. B., Stroynowski, Z. N., et al. (2006). Climate change and coastal hydrographic response along the Atlantic Iberian margin (Tagus Prodelt and Muros Ría) during the last two millennia. *Holocene* 16, 1003–1015. doi:10.1177/0959683606h1990rp
- Liu, J. T., Liu, K. J., and Huang, J. C. (2002). The effect of a submarine canyon on the river sediment dispersal and inner shelf sediment movements in southern Taiwan. *Mar. Geol.* 181, 357–386. doi:10.1016/s0025-3227(01)00219-5
- Liu, X., Rendle-Bühning, R., and Henrich, R. (2016). Climate and sea-level controls on turbidity current activity on the Tanzanian upper slope during the last deglaciation and the Holocene. *Quat. Sci. Rev.* 133, 15–27. doi:10.1016/j.quascirev.2015.12.002
- Lobo, F. J., Goff, J. A., Mendes, I., Bárcenas, P., Fernández-Salas, L. M., Martín-Rosales, W., et al. (2015). Spatial variability of prodeltaic undulations on the Guadalfeo River prodelta: support to the genetic interpretation as hyperpycnal flow deposits. *Mar. Geophys. Res.* 36, 309–333. doi:10.1007/s11001-014-9233-9
- Lobo, F. J., Maldonado, A., Hernández-Molina, F. J., Fernández-Salas, L. M., Ercilla, G., and Alonso, B. (2008). Growth patterns of a proximal terrigenous margin offshore the Guadalfeo River, northern Alboran Sea (SW Mediterranean Sea): glacio-eustatic control and disturbing tectonic factors. *Mar. Geophys. Res.* 29, 195–216. doi:10.1007/S11001-008-9058-5
- López-Avilés, A., García-Alix, A., Jiménez-Moreno, G., Anderson, R. S., Toney, J. L., Mesa-Fernández, J. M., et al. (2021). Latest Holocene paleoenvironmental and paleoclimate reconstruction from an alpine bog in the Western Mediterranean region: the Borreguil de los Lavaderos de la Reina record (Sierra Nevada). *Palaeogeogr. Palaeoclimatol. Palaeoecol.* 573, 110434. doi:10.1016/j.palaeo.2021.110434
- López-González, N., Alonso, B., Juan, C., Ercilla, G., Bozzano, G., Cacho, I., et al. (2019). 133,000 years of sedimentary record in a contourite drift in the Western Alboran Sea: sediment sources and paleocurrent reconstruction. *Geosciences* 9 (8), 345. doi:10.3390/geosciences9080345
- López-Quirós, A., Junna, T., Davies, J., Andresen, K. J., Nielsen, T., Haghypour, N., et al. (2024). Retreat patterns and dynamics of the former Norske Trough Ice Stream (NE Greenland): an integrated geomorphological and sedimentological approach. *Quat. Sci. Rev.* 325, 108477. doi:10.1016/j.quascirev.2023.108477
- López-Quirós, A., Lobo, F. J., Duffy, M., Leventer, A., Evangelinos, D., Escutia, C., et al. (2021). Late Quaternary high-resolution seismic stratigraphy and core-based paleoenvironmental reconstructions in Ona Basin, southwestern Scotia Sea (Antarctica). *Mar. Geol.* 439, 106565. doi:10.1016/j.margeo.2021.106565
- Lowe, D. R. (1979). Sediment gravity flows: their classification and some problems of application to natural flows
- Magny, M. (2004). Holocene climate variability as reflected by mid-European lake-level fluctuations and its probable impact on prehistoric human settlements. *Quat. Int.* 113, 65–79. doi:10.1016/s1040-6182(03)00080-6
- Maillard, A., Gorini, C., Mauffret, A., Sage, F., Lofi, J., and Gaullier, V. (2006). Offshore evidence of polyphase erosion in the Valencia Basin (Northwestern Mediterranean): scenario for the Messinian Salinity Crisis. *Sediment. Geol.* 188–189, 69–91. doi:10.1016/j.sedgeo.2006.02.006
- Martínez-Lamas, R., Toucanne, S., Debret, M., Riboulot, V., Deloffre, J., Boissier, A., et al. (2020). Linking Danube River activity to Alpine Ice-Sheet fluctuations during the last glacial (ca. 33–17 ka BP): insights into the continental signature of Heinrich Stadials. *Quat. Sci. Rev.* 229, 106136. doi:10.1016/j.quascirev.2019.106136
- Martín-Puertas, C., Valero-Garcés, B. L., Mata, M. P., González-Sampériz, P., Bao, R., Moreno, A., et al. (2009). The Iberian–Roman Humid Period (2600–1600 cal yr BP) in the Zofar Lake varve record (Andalucía, southern Spain). *Quat. Res.* 71, 108–120. doi:10.1016/j.yqres.2008.10.004
- Martin-Rosales, W., Pulido-Bosch, A., Vallejos, A., Gisbert, J., Andreu, J. M., and Sanchez-Martos, F. (2007). Hydrological implications of desertification in southeastern Spain. *Hydrol. Sci. J.* 52, 1146–1161. doi:10.1623/hysj.52.6.1146
- Mas, V., Mulder, T., Dennielou, B., Schmidt, S., Khripounoff, A., and Savoye, B. (2010). Multiscale spatio-temporal variability of sedimentary deposits in the Var turbidite system (North-Western Mediterranean Sea). *Mar. Geol.* 275, 37–52. doi:10.1016/j.margeo.2010.04.006
- McCormick, M., Büntgen, U., Cane, M. A., Cook, E. R., Harper, K., Huybers, P., et al. (2012). Climate change during and after the Roman Empire: reconstructing the past from scientific and historical evidence. *J. Interdiscip. Hist.* 43 (2), 169–220. doi:10.1162/jinh_a_00379
- Mena, A., Frances, G., Pérez-Arlucea, M., Aguiar, P., Barreiro-Vazquez, J. D., Iglesias, A., et al. (2015). A novel sedimentological method based on CT-scanning: use for tomographic characterization of the Galicia Interior Basin. *Sediment. Geol.* 321, 123–138. doi:10.1016/j.sedgeo.2015.03.007
- Mendes, I., Dias, J. A., Schönfeld, J., Ferreira, Ó., Rosa, F., Gonzalez, R., et al. (2012). Natural and human-induced Holocene paleoenvironmental changes on the Guadiana shelf (northern Gulf of Cadiz). *Holocene* 22 (9), 1011–1024. doi:10.1177/0959683612437867
- Mendes, I., Lobo, F. J., Fernández-Salas, L. M., López-González, N., Bárcenas, P., Schönfeld, J., et al. (2015). Multi-proxy evidence of rainfall variability recorded in subaqueous deltaic deposits off the Adra River, southeast Iberian Peninsula. *Estuar. Coast. Shelf Sci.* 167 (Pt A), 300–312. doi:10.1016/j.ecss.2015.08.005
- Mendes, I., Lobo, F. J., Hanebuth, T., López-Quirós, A., Schönfeld, J., Lebreiro, S., et al. (2020). Temporal variability of flooding events of Guadiana River (Iberian Peninsula) during the middle to late Holocene: imprints in the shallow-marine sediment record. *Palaeoecology* 556, 109900. doi:10.1016/j.palaeo.2020.109900
- Mesa-Fernández, J. M., Martínez-Ruiz, F., Rodrigo-Gámiz, M., Jiménez-Espejo, F. J., García, M., and Sierro, F. J. (2022). Paleocirculation and paleoclimate conditions in the western Mediterranean basins over the last deglaciation: new insights from sediment composition variations. *Glob. Planet. Change* 209, 103732. doi:10.1016/j.gloplacha.2021.103732
- Micallef, A., Mountjoy, J. J., Canals, M., and Lastras, G. (2012). “Deep-seated bedrock landslides and submarine canyon evolution in an active tectonic margin: Cook Strait, New Zealand,” in *Submarine mass movements and their consequences*. Editors Y. Yamada, K. Kawamura, K. Ikehara, Y. Ogawa, R. Urgeles, and D. Mosher (London: Springer), 201–212.
- Migeon, S., Mulder, T., Savoye, B., and Sage, F. (2012). Hydrodynamic processes, velocity structure and stratification in natural turbidity currents: results inferred from field data in the Var Turbidite System. *Sediment. Geol.* 245–246, 48–62. doi:10.1016/j.sedgeo.2011.12.007
- Millot, C. (2009). Another description of the Mediterranean Sea outflow. *Prog. Oceanogr.* 82 (2), 101–124. doi:10.1016/j.pocan.2009.04.016
- Millot, C. (2014). Heterogeneities of in- and out-flows in the Mediterranean Sea. *Prog. Oceanogr.* 120, 254–278. doi:10.1016/j.pocan.2013.09.007
- Mitchum Jr, R. M. (1985). “Seismic stratigraphic expression of submarine fan,” *Seismic stratigraphy II: an integrated approach to hydrocarbon exploration*. Editors O. R. Berg, and D. G. Woolverton (Tulsa, OK: American Association of Petroleum Geologists, Memoir), 39, 117–136.
- Moernaut, J., Van Daele, M., Heirman, K., Fontijn, K., Strasser, M., Pino, M., et al. (2014). Lacustrine turbidites as a tool for quantitative earthquake reconstruction: new evidence for a variable rupture mode in south central Chile. *J. Geophys. Res. Solid Earth* 119, 1607–1633. doi:10.1002/2013jb010738
- Mojtahid, M., Durand, M., Coste, P.-O., Toucanne, S., Howa, H., Nizou, J., et al. (2018). Millennial-scale Holocene hydrological changes in the northeast Atlantic: new insights from ‘La Grande Vasière’ mid-shelf mud belt. *The Holocene*. 29 (3), 467–480. doi:10.1177/0959683618816478
- Moreno, A., Pérez, A., Frigola, J., Nieto-Moreno, V., Rodrigo-Gámiz, M., Martrat, B., et al. (2012). The medieval climate anomaly in the Iberian Peninsula reconstructed from marine and lake records. *Quat. Sci. Rev.* 43, 16–32. doi:10.1016/j.quascirev.2012.04.007
- Mulder, T., Savoye, B., Piper, D. J. W., and Syvitski, J. P. M. (1998). “The Var submarine sedimentary system: understanding Holocene sediment delivery processes and their importance to the geological record,” *ecological processes on continental margins: sedimentation, mass-wasting and stability*. Editors M. S. Stoker, D. Evans, and A. Cramp (London: Geological Society), 129, 145–166. doi:10.1144/gsl.sp.1998.129.01.10
- Mulder, T., Syvitski, J. P. M., Migeon, S., Faugetes, J. C., and Savoye, B. (2003). Marine hyperpycnal flows: initiation, behavior and related deposits. A review. *Mar. Petroleum Geol.* 20, 861–882. doi:10.1016/j.marpetgeo.2003.01.003
- Muñoz, A., Elvira, E., Leñon, C., Acosta, J., and Jiménez, P. (2017). “Examples of sediment waves in and around submarine canyons of the North Alboran Sea,” in *Atlas of bedforms in the Western Mediterranean*. Editors J. Guillén, J. Acosta, F. L. Chiocci, and A. Palanques (Cham: Springer International Publishing), 247–252.
- Museo de Historia de Motril (2023). Sala de exposiciones. Available online at: <https://cultura.motril.es/red-de-museos/museo-de-historia-de-motril/>.
- Nieto-Moreno, V., Martínez-Ruiz, F., Gallego-Torres, D., Giralt, S., García-Orellana, J., Masqué, P., et al. (2015). Palaeoclimate and palaeoceanographic

- conditions in the westernmost Mediterranean over the last millennium: an integrated organic and inorganic approach. *J. Geol. Soc. Lond.* 172, 264–271. doi:10.1144/jgs2013-105
- Nieto-Moreno, V., Martínez-Ruiz, F., Giral, S., Jiménez-Espejo, F., Gallego-Torres, D., Rodrigo-Gámiz, M., et al. (2011). Tracking climate variability in the western Mediterranean during the Late Holocene: a multiproxy approach. *Clim. Past.* 7, 1395–1414. doi:10.5194/cp-7-1395-2011
- Nieto-Moreno, V., Martínez-Ruiz, F., Willmott, V., García-Orellana, J., Masqué, P., and Damsté, J. S. (2013). Climate conditions in the westernmost Mediterranean over the last two millennia: an integrated biomarker approach. *Org. Geochem.* 55, 1–10. doi:10.1016/j.orggeochem.2012.11.001
- Normark, W. R., and Carlson, P. R. (2003). “Giant submarine canyons: is size any clue to their importance in the rock record?”, *Extreme depositional environments: mega end members in geologic time*. Editors M. A. Chan, and A. W. Archer (Boulder, Colorado: Geological Society of America Special Paper), 370, 170–190. doi:10.1130/0-8137-2370-1.175
- Olariu, C., and Steel, R. J. (2009). Influence of point-source sediment-supply on modern shelf-slope morphology: implications for interpretation of ancient shelf margins. *Basin Res.* 21, 484–501. doi:10.1111/j.1365-2117.2009.00420.x
- Oldfield, F., Asioli, A., Accorsi, C. A., Mercuri, A. M., Juggins, S., Langone, L., et al. (2003). A high resolution late Holocene palaeo-environmental record from the Central Adriatic Sea. *Quat. Sci. Rev.* 22, 319–342. doi:10.1016/s0277-3791(02)00088-4
- Oliva, M., Ruiz-Fernández, J., Barriendos, M., Benito, G., Cuadrat, J. M., Domínguez-Castro, F., et al. (2018). The little ice age in Iberian mountains. *Earth-Sci. Rev.* 177, 175–208. doi:10.1016/j.earscirev.2017.11.010
- Olsen, J., Anderson, N. J., and Knudsen, M. F. (2012). Variability of the North Atlantic oscillation over the past 5,200 years. *Nat. Geosci.* 5, 808–812. doi:10.1038/ngeo1589
- Ortega, J. A., and Garzón, G. (2009). A contribution to improved flood magnitude estimation in base of palaeoflood record and climatic implications – Guadiana River (Iberian Peninsula). *Nat. Hazards Earth Syst. Sci.* 9, 229–239. doi:10.5194/nhess-9-229-2009
- Ortega-Sánchez, M., Lobo, F. J., López-Ruiz, A., Losada, M. A., and Fernández-Salas, L. M. (2014). The influence of shelf-indenting canyons and infralittoral prograding wedges on coastal morphology: the Carchuna system in Southern Spain. *Mar. Geol.* 347, 107–122. doi:10.1016/j.margeo.2013.11.006
- Palanques, A., Guillén, J., Puig, P., and Durrieu de Madron, X. (2008). Storm-driven shelf-to-canyon suspended sediment transport at the southwestern Gulf of Lions. *Cont. Shelf Res.* 28, 1947–1956. doi:10.1016/j.csr.2008.03.020
- Palanques, A., Puig, P., Durrieu de Madron, X., Sanchez-Vidal, A., Pasqual, C., Martín, J., et al. (2012). Sediment transport to the deep canyons and open-slope of the western Gulf of Lions during the 2006 intense cascading and open-sea convection period. *Prog. Oceanogr.* 106, 1–15. doi:10.1016/j.pcean.2012.05.002
- Parrilla, G., and Kinder, T. (1987). Oceanografía física del Mar de Alboran. *Bol. Inst. Esp. Oceanogr.* 4 (1), 133–165.
- Paull, C. K., Caress, D. W., Ussler III, W., Lundsten, E., and Meiner-Johnson, M. (2011). High-resolution bathymetry of the axial channels within Monterey and Soquel submarine canyons, offshore Central California. *Geosphere* 7, 1077–1101.
- Penaud, A., Ganne, A., Eynaud, F., Lambert, C., Coste, P. O., Herlédan, M., et al. (2020). Oceanic versus continental influences over the last 7 kyrs from a mid-shelf record in the northern Bay of Biscay (NE Atlantic). *Quat. Sci. Rev.* 229, 106135–135. doi:10.1016/j.quascirev.2019.106135
- Pérez-Belzuz, F. (1999). Geología del margen y cuenca del mar de alboran durante el plio-cuaternario: sedimentación y tectónica. Ph.D. Thesis Doctoral. Barcelona, Spain: University of Barcelona.
- Pérez-Belzuz, F., and Alonso, B. (2000). Evolución sedimentaria reciente de dos sistemas turbidíticos del área de Motril (NE Alboran). Parte II: Sistema Turbidítico de Sacratif. *Geotemas* 1 (4), 207–211.
- Pérez-Belzuz, F., Alonso, B., and Ercilla, G. (2000). Modelos de sistemas turbidíticos en el área de Motril (NE Alboran). *Geotemas* 1 (4), 213–216.
- Piper, D. J. W., and Normark, W. R. (2009). Processes that initiate turbidity currents and their influence on turbidites: a marine geology perspective. *J. Sediment. Res.* 79 (6), 347–362. doi:10.2110/jsr.2009.046
- Platt, J. P., Whitehouse, M. J., Kelley, S. P., Carter, A., and Hollick, L. (2003). Simultaneous extensional exhumation across the Alboran Basin: implications for the causes of late orogenic extension. *Geology* 31 (3), 251–254. doi:10.1130/0091-7613(2003)031<0251:seeata>2.0.co;2
- Posamentier, H. W., and Vail, P. R. (1988). “Eustatic controls on clastic deposition II: sequence and systems tract models,” *ea level changes: an integrated approach*. Editors C. K. Wilgus, B. S. Hastings, H. Posamentier, J. Van Wagoner, C. A. Ross, and C. G. St. C. Kendall (Tulsa, OK: Society for Sedimentary Geology (SEPM)), 42, 125–154. doi:10.2110/pec.88.01.0125
- Pratson, L. F., and Coakley, B. J. (1996). A model for the headward erosion of submarine canyons induced by downslope-eroding sediment flows. *GSA Bull.* 108, 225–234. doi:10.1130/0016-7606(1996)108<0225:amfthe>2.3.co;2
- Puig, P., Duran, R., Muñoz, A., Elvira, E., and Guillén, J. (2017). Submarine canyon-head morphologies and inferred sediment transport processes in the Alías-Almanzora canyon system (SW Mediterranean): on the role of the sediment supply. *Mar. Geol.* 393, 21–34. doi:10.1016/j.margeo.2017.02.009
- Puig, P., Greenan, B. J. W., Li, M. Z., Prescott, R. H., and Piper, D. J. W. (2013). Sediment transport processes at the head of Halibut Canyon, eastern Canada margin: an interplay between internal tides and dense shelf-water cascading. *Mar. Geol.* 341, 14–28. doi:10.1016/j.margeo.2013.05.004
- Puig, P., Palanques, A., Guillén, J., and El Khatib, M. (2004). Role of internal waves in the generation of nepheloid layers on the northwestern Alboran slope: implications for continental margin shaping. *J. Geophys. Res.* 109, C09011. doi:10.1029/2004JC002394
- Puig, P., Palanques, A., and Martín, J. (2014). Contemporary sediment-transport processes in submarine canyons. *Annu. Rev. Mar. Sci.* 6, 53–77. doi:10.1146/annurev-marine-010213-135037
- Ramos-Román, M. J., Jiménez-Moreno, G., Anderson, R. S., García-Alix, A., Toney, J. L., Jiménez-Espejo, F. J., et al. (2016). Centennial-scale vegetation and North Atlantic oscillation changes during the late Holocene in the southern Iberia. *Quat. Sci. Rev.* 143, 84–95. doi:10.1016/j.quascirev.2016.05.007
- Ramos-Román, M. J., Jiménez-Moreno, G., Camuera, J., García-Alix, A., Anderson, R. S., Jiménez-Espejo, F. J., et al. (2018). Holocene climate aridification trend and human impact interrupted by millennial- and centennial-scale climate fluctuations from a new sedimentary record from Padul (Sierra Nevada, Southern Iberian Peninsula). *Clim. Past.* 14 (1), 117–137. doi:10.5194/cp-14-117-2018
- Regattieri, E., Zanchetta, G., Drysdale, R. N., Isola, I., Hellstrom, J. C., and Dallai, L. (2014). Lateglacial to holocene trace element record (Ba, Mg, Sr) from Corchia cave (Apuan Alps, central Italy): paleoenvironmental implications. *J. Quat. Sci.* 29, 381–392. doi:10.1002/jqs.2712
- Reilly, B. T., Stoner, J. S., and Wiest, J. (2017). SedCT: MATLAB™ tools for standardized and quantitative processing of sediment core computed tomography (CT) data collected using a medical CT scanner. *G-cubed* 18 (8), 3231–3240. doi:10.1002/2017gc006884
- Reimer, P. J., Austin, W. E. N., Bard, E., Bayliss, A., Blackwell, P. G., Bronk Ramsey, C., et al. (2020). The IntCal20 Northern Hemisphere radiocarbon age calibration curve (0–55 cal kBP). *Radiocarbon* 62, 725–757. doi:10.1017/rdc.2020.41
- Reimer, P. J., and McCormac, F. G. (2002). Marine radiocarbon reservoir corrections for the Mediterranean and Aegean Seas. *Radiocarbon* 44, 159–166. doi:10.1017/s0033822200064766
- Reimer, P. J., and Reimer, R. W. (2001). A marine reservoir correction database and on-line interface. *Radiocarbon* 43, 461–463. doi:10.1017/s0033822200038339
- Renault, L., Oguz, T., Pascual, A., Vizoso, G., and Tintore, J. (2012). Surface circulation in the Alborán Sea (western Mediterranean) inferred from remotely sensed data. *J. Geophys. Res. Ocean.* 117 (8), 1–11. doi:10.1029/2011jc007659
- Rodrigo, F. S., Esteban-Parra, M. J., Pozo-Vázquez, D., and Castro-Díez, Y. (1999). A 500-year precipitation record in southern Spain. *Int. J. Climatol.* 19, 1233–1253. doi:10.1002/(sici)1097-0088(199909)19:11<1233::aid-joc413>3.0.co;2-1
- Rodrigo, F. S., and Trigo, R. M. (2007). Trends in daily rainfall in the Iberian Peninsula from 1951 to 2002. *Int. J. Climatol.* 27, 513–529. doi:10.1002/joc.1409
- Rodrigo-Gámiz, M., Martínez-Ruiz, F., Jiménez-Espejo, F. J., Gallego-Torres, D., Nieto-Moreno, V., Romero, O., et al. (2011). Impact of climate variability in the western Mediterranean during the last 20,000 years: oceanic and atmospheric responses. *Quat. Sci. Rev.* 30, 2018–2034. doi:10.1016/j.quascirev.2011.05.011
- Rothwell, R. G., Hoogakker, B. A. A., Thomson, J., and Croudace, I. W. (2006). Turbidite emplacement on the southern Balearic Abyssal Plain (Western Mediterranean Sea) over the last 150 kyr. *J. Geophys. Res.* 111, C06013.
- Rothwell, R. G., and Croudace, I. W. (2015). “Twenty years of XRF core scanning marine sediments: what do geochemical proxies tell us?” in *Micro-XRF studies of sediment cores. Developments in paleoenvironmental research*. Editors I. W. Croudace, and R. G. Rothwell (Dordrecht: Springer Science + Business Media), 25–101.
- Roveri, M., Flecker, R., Krijgsman, W., Lofi, J., Lugli, S., Manzi, V., et al. (2014). The messinian salinity crisis: past and future of a great challenge for marine sciences. *Mar. Geol.* 352, 25–58. doi:10.1016/j.margeo.2014.02.002
- Rueden, C. T., Schindelin, J., Hiner, M. C., DeZonia, B. E., Walter, A. E., Arena, E. T., et al. (2017). ImageJ2: imagej for the next generation of scientific image data. *BMC Bioinforma.* 18, 529. doi:10.1186/s12859-017-1934-z
- Sáez, A., Valero-Garcés, B. L., Giral, S., Moreno, A., Bao, R., Pueyo, J. J., et al. (2009). Glacial to holocene climate changes in the SE Pacific. The raraku lake sedimentary record (Easter Island, 27°S). *Quat. Sci. Rev.* 28, 2743–2759. doi:10.1016/j.quascirev.2009.06.018
- Salabarnada, A., Escutia, C., Roñal, U., Nelson, C. H., McKay, R., Jiménez-Espejo, F. J., et al. (2018). Paleoclimatology and ice sheet variability offshore Wilkes Land, Antarctica - part 1: insights from late Oligocene astronomically paced contourite sedimentation. *Clim. Past* 14, 991–1014. doi:10.5194/cp-14-991-2018
- Saldías, G. S., and Allen, S. E. (2020). The influence of a submarine canyon on the circulation and cross-shore exchanges around an upwelling front. *J. Phys. Oceanogr.* 50, 1677–1698. doi:10.1175/jpo-d-19-0130.1

- Sánchez-García, C., and Schulte, L. (2023). Historical floods in the southeastern Iberian Peninsula since the 16th century: trends and regional analysis of extreme flood events. *Glob. Planet. Change* 231, 104317. doi:10.1016/j.gloplacha.2023.104317
- Sánchez-García, C., Schulte, L., Peña, J. C., Carvalho, F., and Brembilla, C. (2019). 500-year flood history in the arid environments of southeastern Spain. The case of the Almanzora River. *Glob. Planet. Change* 181, 102987. doi:10.1016/j.gloplacha.2019.102987
- Sánchez-López, G., Hernández, A., Pla-Rabes, S., Trigo, R. M., Toro, M., Granados, I., et al. (2016). Climate reconstruction for the last two millennia in central Iberia: the role of East Atlantic (EA), North Atlantic Oscillation (NAO) and their interplay over the Iberian Peninsula. *Quat. Sci. Rev.* 149, 135–150. doi:10.1016/j.quascirev.2016.07.021
- Serrano, M. A., Díez-Minguito, M., Valle-Levinson, A., and Ortega-Sánchez, M. (2020). Circulation in a short, microtidal submarine canyon in the Alboran Sea. *J. Coast. Res.* 95, 1531–1535. doi:10.2112/si95-295.1
- Shepard, F. P. (1981). Submarine canyons: multiple causes and long-time persistence. *Am. Assoc. Petr. Geol. B* 65 (6), 1062–1077. doi:10.1306/03b59459-16d1-11d7-8645000102c1865d
- Siani, G., Paterne, M., Arnold, M., Bard, E., Métivier, B., Tisnérat-Laborde, N., et al. (2000). Radiocarbon reservoir ages in the Mediterranean Sea and Black Sea. *Radiocarbon* 42, 271–280. doi:10.1017/s0033822200059075
- Smith, M. E., Werner, S. H., Buscombe, D., Finnegan, N. J., Sumner, E. J., and Mueller, E. R. (2018). Seeking the shore: evidence for active submarine canyon head incision due to coarse sediment supply and focusing of wave energy. *Geophys. Res. Lett.* 45 (22), 12403–12413. doi:10.1029/2018gl080396
- Sømme, T. O., William, H.-H., Ole, J. M., and John, B. T. (2009). Relationships between morphological and sedimentological parameters in source-to-sink systems: a basis for predicting semi-quantitative characteristics in subsurface systems. *Basin Res.* 21, 361–387. doi:10.1111/j.1365-2117.2009.00397.x
- Sommerfield, C. K., Drake, D. E., and Wheatcroft, R. A. (2002). Shelf record of climatic changes in flood magnitude and frequency, north-coastal California. *Geology* 30, 395–398. doi:10.1130/0091-7613(2002)030<0395:srocci>2.0.co;2
- Sommerfield, C. K., and Wheatcroft, R. A. (2007). Late Holocene sediment accumulation on the northern California shelf: oceanic, fluvial, and anthropogenic influences. *Geol. Soc. Am. Bull.* 119, 1120–1134. doi:10.1130/b26019.1
- Stanley, D. J., Kelling, G., Juan-Antonio Vera, J.-A. V., and Sheng, H. (1975). Sands in the Alboran Sea: a model of input in a deep marine Basin. *Sm. C. Earth S. C.* 15, 1–51.
- Steinke, S., Mohtadi, M., Prange, M., Varma, V., Pittauerova, D., and Fischer, H. W. (2014). Mid-to Late-Holocene Australian–Indonesian summer monsoon variability. *Quat. Sci. Rev.* 93, 142–154. doi:10.1016/j.quascirev.2014.04.006
- Stow, D. A. V., and Smillie, Z. (2020). Distinguishing between deep-water sediment facies: turbidites, contourites and hemipelagites. *Geosciences* 10 (2), 68. doi:10.3390/geosciences10020068
- Stuiver, M., Reimer, P. J., and Reimer, R. W. (2021). Calib 8.2 [WWW program] at J. *Quat. Sci.* 19, 9–21.
- Sweet, M. L., and Blum, M. D. (2016). Connections between fluvial to shallow marine environments and submarine canyons: implications for sediment transfer to deep water. *J. Sediment. Res.* 86 (10), 1147–1162. doi:10.2110/jsr.2016.64
- Talling, P. J., Baker, M. L., Pope, E. L., Ruffell, S. C., Jacinto, R. S., Heijnen, M. S., et al. (2022). Longest sediment flows yet measured show how major rivers connect efficiently to deep sea. *Nat. Commun.* 13, 4193. doi:10.1038/s41467-022-31689-3
- Tarrés, M., Cerdà-Domènech, M., Pedrosa-Pàmies, R., Rumín-Caparrós, A., Calafat, A., Canals, M., et al. (2022). Particle fluxes in submarine canyons along a sediment-starved continental margin and in the adjacent open slope and basin in the SW Mediterranean Sea. *Prog. Oceanogr.* 203, 102783. doi:10.1016/j.pocean.2022.102783
- Thomson, J., Croudace, I. W., and Rothwell, R. G. (2006). “A geochemical application of the ITRAX scanner to a sediment core containing eastern Mediterranean sapropel units,” *ew techniques in sediment core analysis*. Editor R. G. Rothwell (London, United Kingdom: Geological Society of London), 267, 65–77. doi:10.1144/gsl.sp.2006.267.01.05
- Thorndyraft, V. R., and Benito, G. (2006). The Holocene fluvial chronology of Spain: evidence from a newly compiled radiocarbon database. *Quat. Sci. Rev.* 25, 223–234. doi:10.1016/j.quascirev.2005.07.003
- Trouet, V., Esper, J., Graham, N. E., Baker, A., Scourse, J. D., and Frank, D. C. (2009). Persistent positive North Atlantic oscillation mode dominated the medieval climate anomaly. *Science* 324, 78–80. doi:10.1126/science.1166349
- Tucker, M. E. (2001). *Sedimentary petrology: an introduction to the origin of sedimentary rocks*. Oxford: Blackwell Science Ltd., 260.
- Vail, P. R. (1987). “Part 1: seismic stratigraphy interpretation procedure,” *Atlas of Seismic Stratigraphy, volume 1*. Editor A. W. Bally (New York, NY: Springer), 27, 1–10.
- Van Daele, M., Cnudde, V., Duyck, P., Pino, M., Urrutia, R., and De Batist, M. (2014). Multidirectional, synchronously-triggered seismoturbidites and debrites revealed by X-ray computed tomography (CT). *Sedimentology* 61, 861–880. doi:10.1111/sed.12070
- Vis, G.-J., Kasse, C., Kroon, D., Vandenbergh, J., Jung, S., Lebreiro, S. M., et al. (2016). Time-integrated 3D approach of late quaternary sediment-depocenter migration in the tagus depositional system: from river valley to abyssal plain. *Earth Sci. Rev.* 153, 192–211. doi:10.1016/j.earscirev.2015.11.002
- Wacker, L., Bonani, G., Friedrich, M., Hajdas, I., Kromer, B., Nemeč, M., et al. (2010). Micasdas: routine and high-precision radiocarbon dating. *Radiocarbon* 52 (2), 252–262. doi:10.1017/s0033822200045288
- Wacker, L., Fahrni, S. M., Hajdas, I., Molnar, M., Synal, H. A., Szidat, S., et al. (2013a). A versatile gas interface for routine radiocarbon analysis with a gas ion source. *Nucl. Instrum. Methods Phys. Res. Sect. B-Beam Interact. Mater. Atoms* 294, 315–319. doi:10.1016/j.nimb.2012.02.009
- Wacker, L., Lippold, J., Molnar, M., and Schulz, H. (2013b). Towards radiocarbon dating of single Foraminifera with a gas ion source. *Nucl. Instrum. Methods Phys. Res. Sect. B-Beam Interact. Mater. Atoms* 294, 307–310. doi:10.1016/j.nimb.2012.08.038
- Weltje, G. J., and Tjallingii, R. (2008). Calibration of XRF core scanners for quantitative geochemical logging of sediment cores: theory and application. *Earth Planet. Sci. Lett.* 274, 423–438. doi:10.1016/j.epsl.2008.07.054
- Xu, J. P., Barry, J. P., and Paull, C. K. (2013). Small-scale turbidity currents in a big submarine canyon. *Geology* 41, 143–146. doi:10.1130/g33727.1
- Xu, J. P., Wong, F. L., Kvitek, R., Smith, D. P., and Paull, C. K. (2008). Sandwave migration in Monterey Submarine Canyon, central California. *Mar. Geol.* 248 (3–4), 193–212. doi:10.1016/j.margeo.2007.11.005
- Zaragosi, S., Bourillet, J. F., Eynaud, F., Toucanne, S., Denhard, B., Van Toer, A., et al. (2006). The impact of the last European deglaciation on the deep-sea turbidite systems of the celtic-armorican margin (Bay of Biscay). *Geo Mar. Lett.* 26, 317–329. doi:10.1007/s00367-006-0048-9
- Ziegler, M., Jilbert, T., de Lange, G. J., Lourens, L. J., and Reichert, G. (2008). Bromine counts from XRF scanning as an estimate of the marine organic carbon content of sediment cores. *Geochem. Geophys. Geosyst.* 9, Q05009. doi:10.1029/2007gc001932
- Ziegler, M., Lourens, L. J., Tuenter, E., and Reichert, G. J. (2010). High Arabian Sea productivity conditions during MIS 13 – odd monsoon event or intensified overturning circulation at the end of the Mid-Pleistocene transition?. *Clim. Past.* 6, 63–76. doi:10.5194/cp-6-63-2010